Geomechanics and Engineering, *Vol. 43, No. 4 (2025) 281-299*
https://doi.org/10.12989/gae.2025.43.4.281

The effect of bedding plane on the hydraulic fracture growth in gas shale reservoirs: Analytical solution

Jinwei Fu[1], Hadi Haeri[2], Vahab Sarfarazi*[3], Fariborz Matinpoor[4], Shadman Mohammadi Bolbanabad[3], Shirin Jahanmiri[3] and Mohammad Fatehi Marji[5]

[1]*School of Civil Engineering and Transportation, North China University of Water Resources and Electric Power, Zhengzhou, 450046, China*
[2]*Department of Mining Engineering, Higher Education Complex of Zarand, Shahid Bahonar University of Kerman, Kerman, Iran*
[3]*Department of Mining Engineering, Hamedan University of Technology, Hamedan, Iran*
[4]*Department of Mining Engineering, Tehran University, Tehran, Iran*
[5]*Department of Mine Exploitation Engineering, Faculty of Mining and metallurgy, Institute of Engineering, Yazd University, Yazd, Iran*

(*Received February 20, 2023, Revised November 2, 2025, Accepted November 3, 2025*)

Abstract. In the hydraulic fracturing process, the mechanical behavior of bedding planes is known to influence the growth of fractures in the surrounding rock. An analytical investigation was conducted into the growth process of hydraulic fractures in bedded rock. The effects of the number of bedding layers, the mechanical properties of these layers, internal pressure, and confining pressure on radial displacement, radial stress, tangential stress, and the critical radii of failure were examined. In all samples, the bedding planes were oriented perpendicular to the internal pressure. It was observed that as internal pressure increased, radial stress values rose while tangential stress values decreased. When the internal uniform compressive load matched the external load, the values of radial and tangential stresses became independent of radial distance in the cylindrical specimen. It was found that hydraulic fractures (HF) may propagate within the bedding layers due to a decrease in the modulus of elasticity and strength of the rock. Shear failure in the hydraulic fractures was found to be exacerbated when cohesion and friction angle values were low. Numerical simulations indicate that four major sets of tensile fractures developed in a medium strength model, while a significant number of small cracks emerged in the weak rock. The middle layer, which had high tensile strength, remained stable. This suggests that the strong middle layer can transfer internal forces to the weaker rock after crack propagation occurs in the upper layer, resulting in small crack growth in the soft rock. Additionally, the dip angles of the large fracture sets related to the vertical axis were found to be 45 degrees. This study may contribute to the simulation of hydraulic fracturing in oil shale reservoirs.

Keywords: analytical solution; bedding plane; hydraulic fractures; propagation behavior

1. Introduction

Stratification occurs deep within the Earth due to various geological processes. These layers exhibit different mechanical properties and resistances to stress. In hydraulic fracturing tests conducted at these depths, the presence of these layers can significantly influence the test outcomes. This article examines how the material properties of these layers affect the growth and propagation of hydraulic cracks. Shale gas resources are increasingly attracting global attention toward unconventional reservoirs since the conventional hydrocarbon reservoirs are going to be depleted and scarce within a few decades. Shale reservoirs are very dense with low permeability, so that the economic gas and oil production from them permits the conduction of hydraulic fracturing operations. The necessary fractures are generated in the reservoir to achieve a suitable connected fracture network and enhance the gas production by increasing the permeability and seepage channels in the reservoir. In relatively recent challenges, complex fracture networks have developed in the bedded shale reservoirs. The bedding planes are utilized to divert the gases into the channels in the fracture networks provided by hydraulic fracturing techniques (Men *et al.* 2013). Therefore, the proper interactions between the bedding planes of dense shale layers and the complex fracture networks are of utmost importance in the optimized gas production from unconventional gas-shale reservoirs. The mechanisms of interactions between the bedding planes and hydraulic fractures are analyzed through many theoretical, experimental and in situ testing methods (Daneshy 1978, Munoz-Abella *et al.* 2012, Woo *et al.* 2015, Haeri 2015a, b, c, Yaylacı 2016, Shaowei *et al.* 2016, Shuraim *et al.* 2016, Huang *et al.* 2017, Zhang *et al.* 2017, Guo *et al.* 2018, Ajamzadeh *et al.* 2018, Weng *et al.* 2018, Fu *et al.* 2019, Golewski 2019, Banjara *et al.* 2019, Haeri *et al.* 2020, Sarfarazi *et al.* 2021, Naeimi *et al.* 2021, Li *et al.* 2022, Imani *et al.* 2022, Selmi 2022, Wu *et al.* 2022, Zhao *et al.* 2022). For example, the effects of bedding plane inclination angles and the rate of injections in hydraulic fracturing on the mechanisms of crack propagation in the bedded shale reservoirs are discussed by Zhae *et al.* (2022). They claimed

*Corresponding author, Associate Professor
E-mail: sarfarazi@hut.ac.ir

ISSN: 2005-307X (Print), 2092-6219 (Online)

that the fracture pressure may be reduced at high injection rates of fluid. Therefore, optimized low injection rates are more beneficial for hydraulic fracturing in tight gas-shale reservoirs to produce a complex fracture network intersected with the bedding planes. The confining pressure due to in-situ geo-stresses affects the mechanical characteristics of the reservoir rock mass where the hydraulic fracture network is developed. The tri-axial tests are modified to physically model the in-situ hydraulic fracturing tests, considering the real structural conditions of the reservoir rock. However, a large number of specimens and many experimental efforts are needed to convert the study of the hydraulic fracturing under non-confining pressure to that of the real in-situ conditions. Many researchers used the rock-material specimens made from gypsum, cement, concrete, mortar, and other materials to arrange some modified laboratory tests for the real situations, considering the effects of bedding plane and in-situ stresses on the crack propagation mechanisms during the hydro-fracturing operation in shale gas formations. The complex fracture networks considering the limits of the hydraulic fracture expansion and its height within the bedded shales, and also taking into account the effects of bedding planes distances between the shale layers are studied (Huang *et al.* 2017, Weng *et al.* 2018, Wu *et al.* 2022, Li *et al.* 2022). It is concluded that as the strength of the shale and the distance between the layers in a shale formation increase, the hydraulic fracturing capture increases and the complexity of the fracturing network decreases. Huang *et al*. (2017) established three models for fracture propagation mechanisms in hydraulic fracturing operations near the bedding planes by accomplishing the true tri-axial tests. Many scholars numerically modeled these experiments and recognized these three models by simulating the interaction between the hydraulic and natural fractures and bedding planes (Zhang *et al.* 2017, Zhou *et al.* 2017, Cui *et al.* 2018, Guo *et al.* 2018, Fu *et al.* 2019). The three modes of interactions between the natural and hydraulic fractures during a hydraulic fracturing process consist of penetration (crack initiation), diversion, and interactions of offsets (or cracks coalescence phenomena) (Zhang *et al.* 2017, Zhou *et al.* 2017, Cui *et al.* 2018, Fu *et al.* 2019). The difference between in situ stresses and the inclination angles of the hydraulic and natural fractures plays a dominant role in the crack initiation process in these penetration modes of hydraulic fracturing. Natural fractures generally capture the induced hydraulic fractures easily when the differences in horizontal in situ stresses are low and the interaction angles of the hydraulic and natural fractures are relatively small. The other mechanical and geometrical characteristics of the crack propagation and bedding planes in shale reservoirs have been studied at different scales (Cui *et al.* 2018). Huang *et al.* (2017) performed some hydraulic fracturing experiments in a bedded rock and found that the distribution of fracture length in the layered specimens during the experiment depends on the bedding distances, and hydraulic fractures grow in their own directions when the fluid pressure increases to its critical point. The effects of bedding densities on the crack propagation mechanism in hydraulic fracturing were studied experimentally by Guo *et al*. (2018), who deduced that three main interaction modes may exist between the hydraulic fracturing and bedding layers.

However, Bradley *et al.* (2019) explained the fracturing fluid flows through artificial fractures and bedding planes in a laboratory-scale transparent cell. They also checked the effects of proppant viscosities on the migration of fluids from the reservoir to the fracture network. Several numerical approaches have been developed for simulating the hydraulic fracturing tests and considering the effects of bedding planes and inclination angles on the growth of hydraulic fracturing lengths and heights. These numerical approaches produce some proper two or three-dimensional models which demonstrate the fracturing paths and heights and the obstructions causing the leakage of fluids from the bedding planes. In these analyses, the effects of various factors such as spacing of bedding planes, heights, lengths and angles of fractures, fluid injection pressures, injection rates, in situ stress differences, cohesion and friction angle of discontinuity surfaces and the interaction between hydraulic fractures and bedding planes in layered rocks on the hydraulic fracturing process are studied (Zou *et al.* 2016, Akbas 2016, Zeng and Yao 2016, Tang *et al.* 2018, Gong *et al.* 2019, Sun *et al.* 2020, Li *et al.* 2021, Xie *et al.* 2020, Golewski 2023). The current simulation results based on sophisticated numerical methods, such as discrete element methods, show that crack inclination angles and bedding planes' angles have profound effects on the compressive, tensile, and shear strengths of the rocks undergoing the hydraulic fracturing operations. The fracture modes, fracture morphologies, their propagation paths, and fluid flow properties all can be affected by the bedding plane angles and the in-situ stress differences in the bedded rocks. However, in most of these analyses, the mechanical characteristics of the bedding planes on the complex fracture network and their interactions with the natural fractures are not fully considered simultaneously (Woo *et al.* 2015, Yaylacı 2016, Adıyaman *et al.* 2016, Zhang *et al.* 2017, Guo *et al.* 2018, Weng *et al.* 2018, Fu *et al.* 2019, Haeri *et al.* 2020, Sarfarazi *et al.* 2021, Naeimi *et al.* 2021, Li *et al.* 2022, Imani *et al.* 2022, Golewski *et al.* 2022, Öner *et al.* 2022, 2023).

In a fully optimized hydraulic fracturing process in a layered formation, the crack propagation mechanism, the fracture heights and lengths, and the effects of bedding plane properties, including its geometry and mechanical properties, are of great importance and should be used for the simulation and final design of the fracturing operation. In these analyses, further simulation of the hydraulic fracturing process considering different mechanical properties for the bedding planes is developed. The influence of the layers' mechanical behavior on the crack growth mechanism of the hydraulic fractures meeting the bedding planes is evaluated by an analytical procedure. In these simulations, different mechanical properties are considered for the bedding in the layered rock sample. The geometry of the bedding layers is also changed, and the interactions between hydraulic fractures, bedding planes, and natural fractures are considered in the evolution mechanism and crack propagation process of the hydraulic fracture networks.

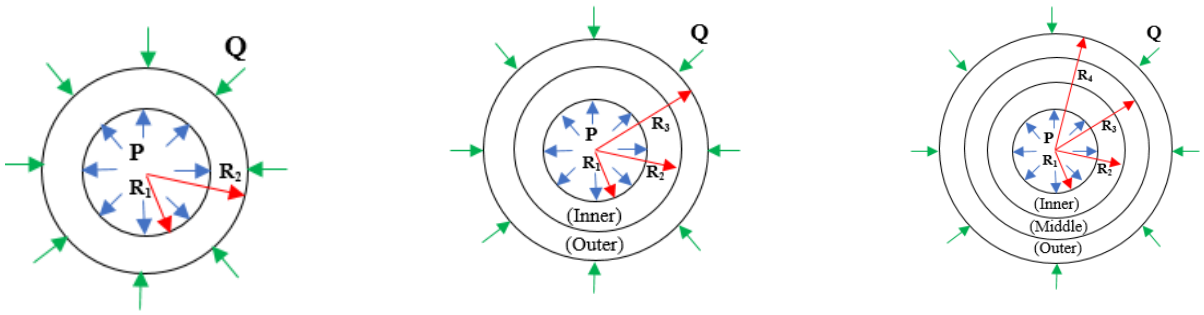

(a) State I (b) State II (c) State III

Fig. 1 Schematic of thick-walled cylindrical rock layers and applied loading system to It, (a) mode I (one-layer model), (b) mode II (2-layer model) and (c) mode III (3-layer model)

2. Determining stress fields and displacement in thick-walled cylindrical rock layers

Fig. 1 shows thick-walled cylinders in 3 states, I, II, and III, which are subjected to internal uniform compressive loads P and external Q. State I shows a rocky material layer with E, σ_C, and υ properties. The inner and outer radii of the cylindrical stone layer, in this case, are equal to R1 and R2, respectively. In case II, another cylindrical stone layer with EO ‹σ_{co} , υ_O characteristics (O index indicates the externality of the cylinder) whose inner and outer radii are equal to R2 and R3, respectively, surrounds the outer boundary of the inner material. In mode III, similar to mode II, another layer with different characteristics from the inner and middle layers, whose inner and outer radii are equal to R3 and R4, respectively, surrounds the inner two layers. The interface conditions between the layers in composite states II and III are considered a "fully bonded interface (Sadd 2020). Considering such an assumption, the fields of displacement and stress at the interface of two completely bonded materials will be continuous. In this study, the aim is to determine the stress and displacement fields in the cylindrical rock layers of the shape that we described. According to the geometry of the problem and assuming the plane strain (the length of the third-dimension perpendicular to the plane, which is in the z direction), in order to obtain the stress and displacement fields, polar coordinates should be used.

It can be seen that the problem in question has axial symmetry. Therefore, the tangential displacement is zero ($u\theta=0$). Also, the radial displacement is only a function of the radial distance r; that means (Sadd 2020)

$$u_r = u_r(r) \tag{1}$$

Therefore, the displacement vector in this problem only includes the radial component of the displacement field. As a result, the stress fields are only dependent on r and will be independent of θ.

According to the topics of elasticity theory, stress fields in polar coordinates are equal to (Sadd 2020)

In the above relations, it is a function of Airy stress. Considering that the field of displacement and stress is independent of θ, which was mentioned earlier, the Airy

$$\begin{aligned}\sigma_r &= \frac{1}{r}\frac{\partial\phi}{\partial r}+\frac{1}{r^2}\frac{\partial^2\phi}{\partial\theta^2}\\ \sigma_\theta &= \frac{\partial^2\phi}{\partial r^2}\\ \tau_{r\theta} &= -\frac{\partial}{\partial r}\left(\frac{1}{r}\frac{\partial\phi}{\partial\theta}\right)\end{aligned} \tag{2}$$

stress function suitable for solving this problem should also be independent of θ. Therefore, the triple relation (2) is rewritten as follows

$$\begin{aligned}\sigma_r &= \frac{1}{r}\frac{\partial\phi}{\partial r}\\ \sigma_\theta &= \frac{\partial^2\phi}{\partial r^2}\\ \tau_{r\theta} &= 0\end{aligned} \tag{3}$$

The Airy stress function related to this problem will be equal to (Sadd 2020)

$$\phi = a_0 + a_1\log r + a_2 r^2 + a_3 r^2\log r \tag{4}$$

When the body contains the coordinate origin, the coefficients a1 and a3 must be zero so that the stress field remains limited. Also, if the geometry of the area is such that the origin of the coordinates (in this case, the center of the cylinders) can be surrounded by any curve that is completely inside the area, term a3 leads to multi-valued behavior in the change of peripheral location. Therefore, in this problem, the coefficient of a3 must be equal to zero. As a result, the Airy stress function of relation (4) can be rewritten as follows

$$\phi = a_0 + a_1\log r + a_2 r^2 \tag{5}$$

By placing the Airy stress function of relation (5) in the relations of the stress field, we will have relation (6)

$$\begin{aligned}\sigma_r &= \frac{1}{r}\left(\frac{a_1}{r}+2a_2 r\right)=\frac{a_1}{r^2}+2a_2\\ \sigma_\theta &= -\frac{a_1}{r^2}+2a_2\\ \tau_{r\theta} &= 0\end{aligned} \tag{6}$$

Ignoring the field of radial and tangential stresses, Eq. (6) can be rewritten as Eq. (7)

$$\begin{aligned}\sigma_r &= \frac{A}{r^2}+B\\ \sigma_\theta &= -\frac{A}{r^2}+B\end{aligned} \tag{7}$$

On the other hand, considering the assumption of plane strain, the stress perpendicular to the zσ plane using Hooke's law and inserting the radial and tangential stress values from Eq. (7) will be equal to

$$\varepsilon_z = 0 \Rightarrow \frac{1}{E}\left[\sigma_z - \upsilon(\sigma_r + \sigma_\theta)\right] = 0 \Rightarrow \sigma_z = 2\upsilon B \tag{8}$$

Also, radial and tangential strain fields according to the concepts of material resistance and elasticity theory are equal to (Sadd 2020)

$$\begin{cases} \varepsilon_r = \dfrac{\partial u_r}{\partial r} \Rightarrow \dfrac{1}{E}\left[\sigma_r - \upsilon(\sigma_\theta + \sigma_z)\right] = \dfrac{\partial u_r}{\partial r} \\ \varepsilon_\theta = \dfrac{u_r}{r} \Rightarrow \dfrac{1}{E}\left[\sigma_\theta - \upsilon(\sigma_r + \sigma_z)\right] = \dfrac{u_r}{r} \end{cases} \tag{9}$$

By substituting the radial and tangential stress fields from Eq. (7) into Eq. (9) and subsequently performing the necessary simplifications, we obtain

$$u_r = \frac{(1+\upsilon)}{E} r\left[-\frac{A}{r^2} + (1-2\upsilon)B\right] \tag{10}$$

In the relations obtained for the radial and tangential stresses as well as the radial displacement, the constants A and B are unknown. To obtain these constants, the boundary conditions of stress or displacement must be applied according to different states I, II, and III. In the following, we obtain the stress fields and unknown constants for each of the mentioned states.

2.1 Single layer model (mode I)

In this case, the stress and displacement fields will be in the form of relation (11)

$$\begin{aligned} \sigma_r &= \frac{A}{r^2} + B \\ \sigma_\theta &= -\frac{A}{r^2} + B \\ u_r &= \frac{(1+\upsilon)}{E} r\left[-\frac{A}{r^2} + (1-2\upsilon)B\right] \end{aligned} \tag{11}$$

In the ternary relationship (11), the constants A and B are unknown. In this case, we have 2 boundary conditions related to radial stresses. By applying the mentioned boundary conditions, the values of parameters A and B are obtained as follows

$$\begin{cases} \left.\begin{aligned} &\sigma_r(R_1) = -P \Rightarrow \frac{A}{R_1^2} + B = -P \\ &\sigma_r(R_2) = Q \Rightarrow \frac{A}{R_2^2} + B = -Q \end{aligned}\right\} \Rightarrow \\ \begin{cases} A = \dfrac{(Q-P)R_1^2 R_2^2}{(R_2^2 - R_1^2)} \\ B = \dfrac{PR_1^2 - QR_2^2}{(R_2^2 - R_1^2)} \end{cases} \end{cases} \tag{12}$$

Finally, by placing parameters A and B from relation (12) in the three relations (11), the equations of radial stress, tangential stress and radial displacement are obtained as follows

$$\begin{aligned} \sigma_r &= \frac{(Q-P)R_1^2 R_2^2}{(R_2^2 - R_1^2)} \frac{1}{r^2} + \frac{PR_1^2 - QR_2^2}{(R_2^2 - R_1^2)} \\ \sigma_\theta &= -\frac{(Q-P)R_1^2 R_2^2}{(R_2^2 - R_1^2)} \frac{1}{r^2} + \frac{PR_1^2 - QR_2^2}{(R_2^2 - R_1^2)} \\ u_r &= \frac{(1+\upsilon)}{E} r\left[-\frac{(Q-P)R_1^2 R_2^2}{(R_2^2 - R_1^2)} \frac{1}{r^2} + \frac{(1-2\upsilon)(PR_1^2 - QR_2^2)}{(R_2^2 - R_1^2)}\right] \end{aligned} \tag{13}$$

2.2 Two-layer model (mode II)

In this case, the stress and displacement fields in the inner and outer layers can be represented as a set of relations (14)

$$\begin{cases} \sigma_r^{(I)} = \dfrac{A^{(I)}}{r^2} + B^{(I)} \\ \sigma_\theta^{(I)} = -\dfrac{A^{(I)}}{r^2} + B^{(I)} \\ u_r^{(I)} = \dfrac{(1+\upsilon_I)}{E_I} r\left[-\dfrac{A^{(I)}}{r^2} + (1-2\upsilon_I)B^{(I)}\right] \end{cases} ; \quad \begin{cases} \sigma_r^{(O)} = \dfrac{A^{(O)}}{r^2} + B^{(O)} \\ \sigma_\theta^{(O)} = -\dfrac{A^{(O)}}{r^2} + B^{(O)} \\ u_r^{(O)} = \dfrac{(1+\upsilon_O)}{E_O} r\left[-\dfrac{A^{(O)}}{r^2} + (1-2\upsilon_O)B^{(O)}\right] \end{cases} \tag{14}$$

In the above relationships, the superscripts and indices I and O are related to the inner and outer cylinders, respectively. In this case, we have 4 unknown parameters including $A^{(I)}$ $B^{(I)}$ ، $A^{(O)}$ ،and $B^{(O)}$. On the other hand, we have 4 boundary conditions, 2 of which are related to the equality of radial stresses in the internal boundary of the internal material and the external boundary of the external material. By applying them, the values of the parameters and can be written according to the set of relations (15)

$$\begin{cases} \sigma_r^{(I)}(R_1) = -P \Rightarrow \dfrac{A^{(I)}}{R_1^2} + B^{(I)} = \\ -P \Rightarrow B^{(I)} = -\left(P + \dfrac{A^{(I)}}{R_1^2}\right) \\ \sigma_r^{(O)}(R_3) = -Q \Rightarrow \dfrac{A^{(O)}}{R_3^2} + B^{(O)} = \\ -Q \Rightarrow B^{(O)} = -\left(Q + \dfrac{A^{(O)}}{R_3^2}\right) \end{cases} \tag{15}$$

By placing the values of parameters $B^{(I)}$ and $B^{(O)}$ from Eq. (15) in the equations of radial stress, tangential stress and change of radial position in inner and outer cylinders, Eq. (14) can be rewritten as Eq. (16)

$$\begin{cases} \sigma_r^{(I)} = \dfrac{A^{(I)}}{r^2} - \dfrac{A^{(I)}}{R_1^2} - P \\ \sigma_\theta^{(I)} = -\dfrac{A^{(I)}}{r^2} - \dfrac{A^{(I)}}{R_1^2} - P \\ u_r^{(I)} = \dfrac{(1+\upsilon_I)}{E_I} r\left[-\dfrac{A^{(I)}}{r^2} - (1-2\upsilon_I)\left(\dfrac{A^{(I)}}{R_1^2} + P\right)\right] \end{cases} \quad \& \quad \begin{cases} \sigma_r^{(O)} = \dfrac{A^{(O)}}{r^2} - \dfrac{A^{(O)}}{R_3^2} - Q \\ \sigma_\theta^{(O)} = -\dfrac{A^{(O)}}{r^2} - \dfrac{A^{(O)}}{R_3^2} - Q \\ u_r^{(O)} = \dfrac{(1+\upsilon_O)}{E_O} r\left[-\dfrac{A^{(O)}}{r^2} - (1-2\upsilon_O)\left(\dfrac{A^{(O)}}{R_3^2} + Q\right)\right] \end{cases} \tag{16}$$

On the other hand, at the interface of two inner and outer cylinders, the radial stresses and radial displacements

must be equal, so we will have 2 more boundary conditions according to the set of relations (17)

$$\begin{cases} \sigma_r^{(I)}(R_2)=\sigma_r^{(O)}(R_2)\Rightarrow A^{(I)}\left(\frac{1}{R_2^{\,2}}-\frac{1}{R_1^{\,2}}\right)-P \\ =A^{(O)}\left(\frac{1}{R_2^{\,2}}-\frac{1}{R_3^{\,2}}\right)-Q \\ u_r^{(I)}(R_2)=u_r^{(O)}(R_2)\Rightarrow \frac{(1+\upsilon_I)}{E_I}R_2 \\ \left[-\frac{A^{(I)}}{R_2^{\,2}}-(1-2\upsilon_I)\left(\frac{A^{(I)}}{R_1^{\,2}}+P\right)\right]= \\ \frac{(1+\upsilon_O)}{E_O}R_2\left[-\frac{A^{(O)}}{R_2^{\,2}}-(1-2\upsilon_O)\left(\frac{A^{(O)}}{R_3^{\,2}}+Q\right)\right] \end{cases} \tag{17}$$

By rewriting the set of relations (18), we will arrive at a device of 2 equations with 2 unknowns as follows

$$\begin{cases} \left(\frac{1}{R_2^{\,2}}-\frac{1}{R_1^{\,2}}\right)A^{(I)}-\left(\frac{1}{R_2^{\,2}}-\frac{1}{R_3^{\,2}}\right)A^{(O)}=(P-Q) \\ \left(\frac{1}{R_2^{\,2}}+\frac{(1-2\upsilon_I)}{R_1^{\,2}}\right)\left(\frac{1+\upsilon_I}{E_I}\right)A^{(I)}- \\ \left(\frac{1}{R_2^{\,2}}+\frac{(1-2\upsilon_O)}{R_3^{\,2}}\right)\left(\frac{1+\upsilon_O}{E_O}\right)A^{(O)}= \\ \left(\frac{(1+\upsilon_O)(1-2\upsilon_O)}{E_O}Q-\frac{(1+\upsilon_I)(1-2\upsilon_I)}{E_O}P\right) \end{cases} \tag{18}$$

Which by solving those parameters $A^{(I)}$ and $A^{(O)}$ are equal to

$$A^{(I)}=\left(\frac{R_1^{\,2}}{R_3^{\,2}}\right)\left(\frac{R_3^{\,2}-R_2^{\,2}}{R_1^{\,2}-R_2^{\,2}}\right)A^{(O)}+\left(\frac{R_1^{\,2}R_2^{\,2}}{R_1^{\,2}-R_2^{\,2}}\right)(P-Q)$$

$$A^{(O)}=R_2^{\,2}R_3^{\,2}\left(\begin{array}{l}\left[\begin{array}{l}\left(\frac{E_I}{E_O}\right)\left(\frac{1+\upsilon_O}{1+\upsilon_I}\right)(1-2\upsilon_O)+ \\ \left(\frac{R_1^{\,2}+R_2^{\,2}(1-2\upsilon_I)}{R_1^{\,2}-R_2^{\,2}}\right)\end{array}\right]Q- \\ \frac{\left[(1-2\upsilon_I)+\left(\frac{R_1^{\,2}+R_2^{\,2}(1-2\upsilon_I)}{R_1^{\,2}-R_2^{\,2}}\right)\right]P}{\left[\begin{array}{l}\left(R_1^{\,2}+R_2^{\,2}(1-2\upsilon_I)\right)\left(\frac{R_3^{\,2}-R_2^{\,2}}{R_1^{\,2}-R_2^{\,2}}\right)- \\ \left(R_3^{\,2}+R_2^{\,2}(1-2\upsilon_O)\right)\left(\frac{E_I}{E_O}\right)\left(\frac{1+\upsilon_O}{1+\upsilon_I}\right)\end{array}\right]}\end{array}\right) \tag{19}$$

2.3 Three-layer model (mode III)

In this case, the stress and radial displacement fields in the inner, middle and outer cylinders can be represented as a set of relations (20), (21) and (22)

$$\begin{cases} \sigma_r^{(I)}=\frac{A^{(I)}}{r_I^{\,2}}+B^{(I)} \\ \sigma_\theta^{(I)}=-\frac{A^{(I)}}{r_I^{\,2}}+B^{(I)} \\ u_r^{(I)}=\frac{(1+\upsilon_I)}{E_I}r_I \\ \left[-\frac{A^{(I)}}{r_I^{\,2}}+(1-2\upsilon_I)B^{(I)}\right] \end{cases} \quad ; \quad R_1\le r_I\le R_2 \tag{20}$$

$$\begin{cases} \sigma_r^{(M)}=\frac{A^{(M)}}{r_M^{\,2}}+B^{(M)} \\ \sigma_\theta^{(M)}=-\frac{A^{(M)}}{r_M^{\,2}}+B^{(M)} \\ u_r^{(M)}=\frac{(1+\upsilon_M)}{E_M}r_M \\ \left[-\frac{A^{(M)}}{r_M^{\,2}}+(1-2\upsilon_M)B^{(M)}\right] \end{cases} \quad ; \quad R_2\le r_M\le R_3 \tag{21}$$

$$\begin{cases} \sigma_r^{(O)}=\frac{A^{(O)}}{r_O^{\,2}}+B^{(O)} \\ \sigma_\theta^{(O)}=-\frac{A^{(O)}}{r_O^{\,2}}+B^{(O)} \\ u_r^{(O)}=\frac{(1+\upsilon_O)}{E_I}r_O \\ \left[-\frac{A^{(O)}}{r_O^{\,2}}+(1-2\upsilon_O)B^{(O)}\right] \end{cases} \quad ; \quad R_3\le r_O\le R_4 \tag{22}$$

In this case, we have 6 unknown parameters including $A^{(I)}$ $B^{(M)}$ ، $B^{(I)}$ ، $A^{(O)}$ ، $A^{(M)}$ ،and $B^{(O)}$ On the other hand, we have 6 boundary conditions, 2 of which are related to the radial stresses in the internal boundary of the internal material and the external boundary of the external material. By applying them, the values of the parameters $B^{(I)}$ and $B^{(O)}$ can be written according to $A^{(I)}$ andin the dual $A^{(O)}$ Eq. (23)

$$\begin{cases} \sigma_r^{(I)}(R_1)=-P\Rightarrow\frac{A^{(I)}}{R_1^{\,2}}+B^{(I)}= \\ -P\Rightarrow B^{(I)}=-\left(P+\frac{A^{(I)}}{R_1^{\,2}}\right) \\ \sigma_r^{(O)}(R_4)=-Q\Rightarrow\frac{A^{(O)}}{R_4^{\,2}}+B^{(O)}= \\ -Q\Rightarrow B^{(O)}=-\left(Q+\frac{A^{(O)}}{R_4^{\,2}}\right) \end{cases} \tag{23}$$

By placing the values of parameters $B^{(I)}$ and $B^{(O)}$ from Eq. (23) in the stress and displacement equations of Eqs. (20) and (22) related to internal and external cylinders, these relations can be rewritten as follows

$$\begin{cases} \sigma_r^{(I)}=\frac{A^{(I)}}{r_I^{\,2}}-\frac{A^{(I)}}{R_1^{\,2}}-P \\ \sigma_\theta^{(I)}=-\frac{A^{(I)}}{r_I^{\,2}}-\frac{A^{(I)}}{R_1^{\,2}}-P \\ u_r^{(I)}=\frac{(1+\upsilon_I)}{E_I}r_I \\ \left[-\frac{A^{(1)}}{r_I^{\,2}}-(1-2\upsilon_I)\left(\frac{A^{(I)}}{R_1^{\,2}}+P\right)\right] \end{cases} \quad ; \quad R_1\le r_I\le R_2 \tag{24}$$

$$\begin{cases} \sigma_r^{(O)}=\frac{A^{(O)}}{r_O^{\,2}}-\frac{A^{(O)}}{R_4^{\,2}}-Q \\ \sigma_\theta^{(O)}=-\frac{A^{(O)}}{r_O^{\,2}}-\frac{A^{(O)}}{R_4^{\,2}}-Q \\ u_r^{(O)}=\frac{(1+\upsilon_O)}{E_O}r_O \\ \left[\begin{array}{l}-\frac{A^{(O)}}{r_O^{\,2}}- \\ (1-2\upsilon_O)\left(\frac{A^{(O)}}{R_4^{\,2}}+Q\right)\end{array}\right] \end{cases} \quad ; \quad R_3\le r_O\le R_4 \tag{25}$$

On the other hand, the radial stresses and radial displacements must be equal at the boundary between the inner and middle cylinders, as well as the boundary between the middle and outer cylinders, so we will have 4 other boundary conditions as follows

$$\begin{cases} \sigma_r^{(I)}(R_2)=\sigma_r^{(M)}(R_2)\Rightarrow A^{(I)}\left(\frac{1}{R_2^{\,2}}-\frac{1}{R_1^{\,2}}\right)-P \\ =\frac{A^{(M)}}{R_2^{\,2}}+B^{(M)} \\ \sigma_r^{(M)}(R_3)=\sigma_r^{(O)}(R_3)\Rightarrow \frac{A^{(M)}}{R_3^{\,2}}+B^{(M)}= \\ A^{(O)}\left(\frac{1}{R_3^{\,2}}-\frac{1}{R_4^{\,2}}\right)-Q \end{cases} \tag{26}$$

$$\begin{cases} u_r^{(I)}(R_2)=u_r^{(M)}(R_2)\Rightarrow \frac{(1+\upsilon_I)}{E_I}R_2 \\ \left[-\frac{A^{(I)}}{R_2^{\,2}}-(1-2\upsilon_I)\left(\frac{A^{(I)}}{R_1^{\,2}}+P\right)\right]= \\ \frac{(1+\upsilon_M)}{E_M}R_2\left[-\frac{A^{(M)}}{R_2^{\,2}}+(1-2\upsilon_M)B^{(M)}\right] \\ u_r^{(M)}(R_3)=u_r^{(O)}(R_3)\Rightarrow \frac{(1+\upsilon_M)}{E_M}R_3\left[-\frac{A^{(M)}}{R_3^{\,2}}+\right. \\ \left.(1-2\upsilon_M)B^{(M)}\right] \\ =\frac{(1+\upsilon_O)}{E_O}R_3\left[-\frac{A^{(O)}}{R_3^{\,2}}-(1-2\upsilon_O)\left(\frac{A^{(O)}}{R_4^{\,2}}+Q\right)\right] \end{cases} \tag{27}$$

From the boundary conditions related to the equality of radial stress at the boundary between the inner and middle cylinders as well as the middle and outer cylinders of Eq. (26), the parameters $A^{(I)}$ and $A^{(O)}$ can be written according to $A^{(M)}$ and $B^{(M)}$ in the form of Eq. (28)

$$\begin{cases} A^{(I)}=\left(\frac{R_1^{\,2}R_2^{\,2}}{R_1^{\,2}-R_2^{\,2}}\right)\left(\frac{A^{(M)}}{R_2^{\,2}}+B^{(M)}+P\right) \\ A^{(O)}=\left(\frac{R_3^{\,2}R_4^{\,2}}{R_4^{\,2}-R_3^{\,2}}\right)\left(\frac{A^{(M)}}{R_3^{\,2}}+B^{(M)}+Q\right) \end{cases} \tag{28}$$

By inserting the parameters $A^{(I)}$ and $A^{(O)}$ from Eq. (28) into Eq. (27) related to the equality of the change of radial locations at the border between the inner and middle cylinders as well as the middle and outer cylinders, we will reach the following equation system

$$\begin{cases} aA^{(M)}+bB^{(M)}=c \\ a'A^{(M)}+b'B^{(M)}=c' \end{cases} \tag{29}$$

Table 1 Average value of the physical and geomechanical parameters of materials

parameters	Symbol	Value			Unit
		Number of Material			
		(1)	(2)	(3)	
Modulus of Elasticity	E	1.2	4	8	GPa
Uniaxial Compressive Strength	σ_c	2	6	13	MPa
Tension strength	σ_t	0.15	0.6	0.8	MPa
Cohesion Strength	C	0.6	2	5	MPa
Friction Angle	ϕ	34	38	42	(°)
Poisson Ratio	υ	0.3	0.24	0.2	-

By solving the Eq. (29), the parameters $A^{(M)}$ and $B^{(M)}$ are obtained as follows

$$\begin{cases} A^{(M)}=\frac{(cb'-bc')}{(ab'-ba')} \\ B^{(M)}=\frac{(ac'-ca')}{(ab'-ba')} \end{cases} \tag{30}$$

In relation (29) and (30), parameters a, b, c, a′, b′ and c′ are equal to

$$\begin{cases} a=\left(\frac{1}{R_2^{\,2}}\right)\left[\frac{(1+\upsilon_I)}{E_I}\left(\frac{R_1^{\,2}+(1-2\upsilon_I)R_2^{\,2}}{R_1^{\,2}-R_2^{\,2}}\right)-\frac{(1+\upsilon_M)}{E_M}\right] \\ b=\left[\frac{(1+\upsilon_I)}{E_I}\left(\frac{R_1^{\,2}+(1-2\upsilon_I)R_2^{\,2}}{R_1^{\,2}-R_2^{\,2}}\right)+\frac{(1+\upsilon_M)(1-2\upsilon_M)}{E_M}\right] \\ c=-\frac{2\left(1-\upsilon_I^{\,2}\right)R_1^{\,2}}{E_I\left(R_1^{\,2}-R_2^{\,2}\right)}P \end{cases} ; \tag{31}$$

$$\begin{cases} a'=\left(\frac{1}{R_3^{\,2}}\right)\left[\frac{(1+\upsilon_O)}{E_O}\left(\frac{R_4^{\,2}+(1-2\upsilon_O)R_3^{\,2}}{R_4^{\,2}-R_3^{\,2}}\right)-\frac{(1+\upsilon_M)}{E_M}\right] \\ b'=\left[\frac{(1+\upsilon_O)}{E_O}\left(\frac{R_4^{\,2}+(1-2\upsilon_O)R_3^{\,2}}{R_4^{\,2}-R_3^{\,2}}\right)+\frac{(1+\upsilon_M)(1-2\upsilon_M)}{E_M}\right] \\ c'=-\frac{2\left(1-\upsilon_O^{\,2}\right)R_4^{\,2}}{E_O\left(R_4^{\,2}-R_3^{\,2}\right)}Q \end{cases}$$

Finally, by substituting the values of parameters $A^{(M)}$ and $B^{(M)}$ from relation (30) in dual relations (28), the values of parameters $A^{(I)}$ and $A^{(O)}$ are obtained. After that, by placing the parameters $A^{(I)}$ and $A^{(O)}$ from the Eq. (28), the parameters $B^{(I)}$ and $B^{(O)}$ are obtained, respectively, in the dual relations (23).

Sensitivity analysis:

In order to investigate the effect of different parameters on the values of radial and tangential stress as well as the change of radial displacement in different states (I, II, and III), 3 materials with different physical and geomechanical parameter values have been considered according to Table 1. Table 2 presents the values of uniform compressive loads applied to the inner and outer borders of the cylinders as well as their inner and outer radii. Based on the values of the available parameters in Tables 1 and 2, all the diagrams are drawn in the 3 models and also in failure mode. In the following, diagrams related to single-layer, two-layer, and 3-layer models are drawn, followed by diagrams related to the failure mode, taking into account the Mohr-Coulomb criterion. Also, in each section, the behavior of the graphs is analyzed.

Table 2 The values of loads applied to Cylinders and the Geometrical parameters of them

parameters	Symbol	Value	Unit
Uniform internal pressure load	P	2	MPa
Uniform external pressure load	Q	8	MPa
Inner radius of cylinder 1	R_1	1.5	m
Outer radius of cylinder 1 or inner radius of cylinder 2	R_2	4	m
Outer radius of cylinder 2 or inner radius of cylinder 3	R_3	7	m
Outer radius of cylinder 3	R_4	10	m

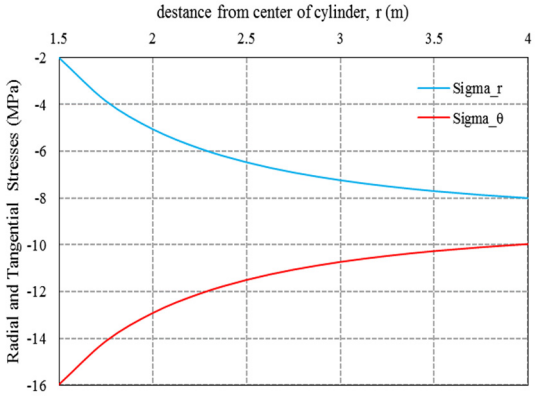

Fig. 2 Field of radial and tangential stresses for 3 materials with different characteristics in the single layer model

2.4 Diagrams of the single layer model (mode I)

Fig. 2 shows the field of radial and tangential stresses inside materials (1), (2), and (3). In all 3 materials, the values of the radial and tangential stress fields are the same. The reason for this is that the stress field in the single-layer model is independent of the material properties according to the set of relations (11). Also, the negativity of the stress values shows that the stress is of a compressive type.

Fig. 3 shows the radial displacements in materials (1), (2), and (3) with different elasticity moduli and Poisson's ratios according to Table 1. As can be seen, in general, by moving away from the center of the thick-walled cylinders (by moving from the inner border of the thick-walled stone cylinders towards their outer border), the radial displacements also increase. In addition, it can be seen from the graphs that materials with a lower modulus of elasticity show larger radial displacements.

Figs. 4 and 5 show the effect of a uniform compressive load applied to the outer boundary of the stone cylinder on the radial and tangential stresses, respectively. As can be seen from Figs. 4 and 5, with the increase of uniform external compressive load, the values of radial and tangential stresses in the rock cylinder increase. When the uniform compressive load applied to the outer boundary of the cylinder is equal to the uniform compressive load applied to the inner boundary (P = Q = 2 MPa), the values of radial and tangential stresses remain constant regardless of the radial distance from the center of the cylinder. Along

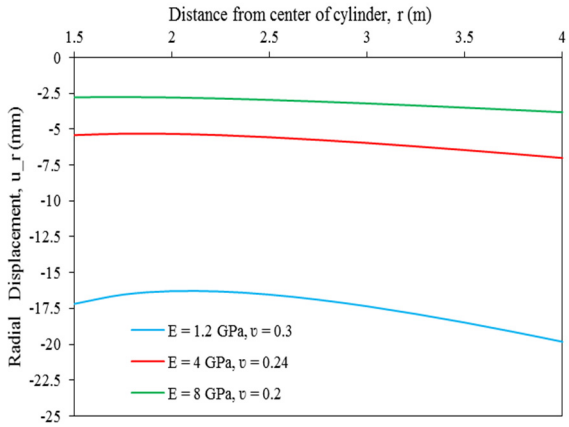

Fig. 3 Radial displacements in 3 different materials in the single layer model

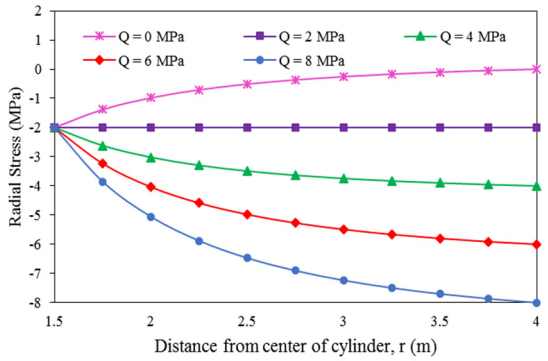

Fig. 4 Variations of radial stress relative to the distance from the center of the cylinder for different values of uniform compressive load applied to the outer boundary of the cylinder in the single layer model

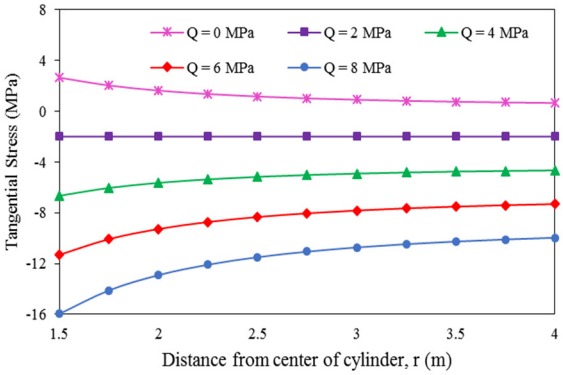

Fig. 5 Changes in tangential stress relative to the distance from the center of the cylinder for different values of uniform compressive load applied to the outer boundary of the cylinder in the single-layer model

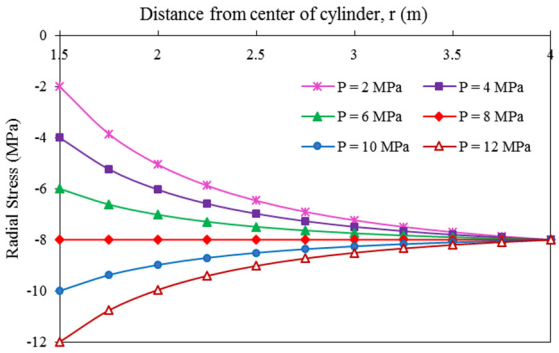

Fig. 6 Comparison of radial stress at various positions along the radius of the cylinder under different uniform compressive forces exerted on the inner boundary of the single-layer model

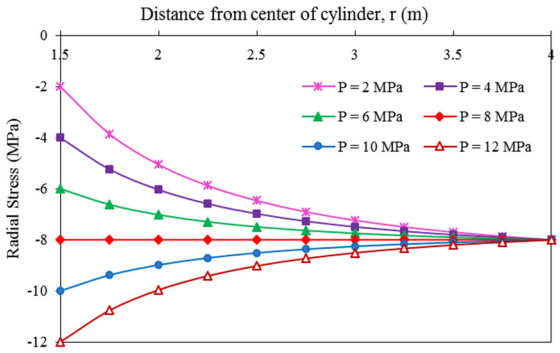

Fig. 6 Comparison of radial stress at various positions along the radius of the cylinder under different uniform compressive forces exerted on the inner boundary of the single-layer model

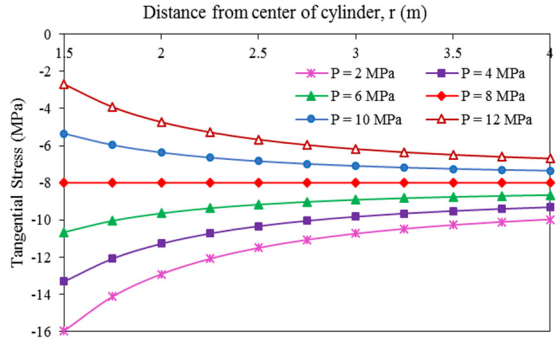

Fig. 7 Comparison of tangential stress at various positions along the radius of the cylinder under different uniform compressive forces exerted on the inner boundary of the single-layer model

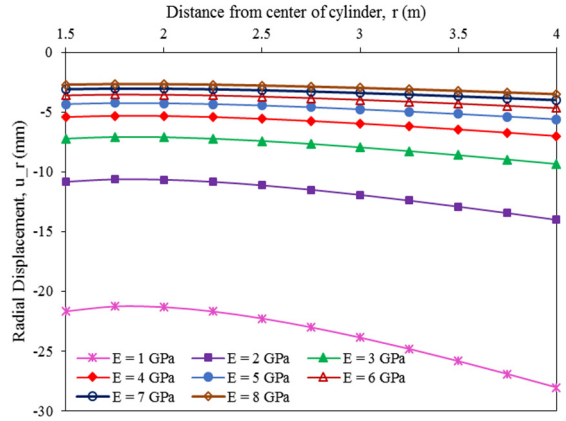

Fig. 8 Variations of radial displacement with respect to the distance from the center of the cylinder for Poisson's ratio of 0.24 and different values of modulus of elasticity from 10 Gpa to 80 Gpa in the single layer model

the path from the inner radius to the outer radius of the cylinder, these stresses are fixed and equal to the applied pressure load of 2 MPa.

Figs. 6 and 7 show the effect of uniform compressive load applied to the inner boundary of the stone cylinder on

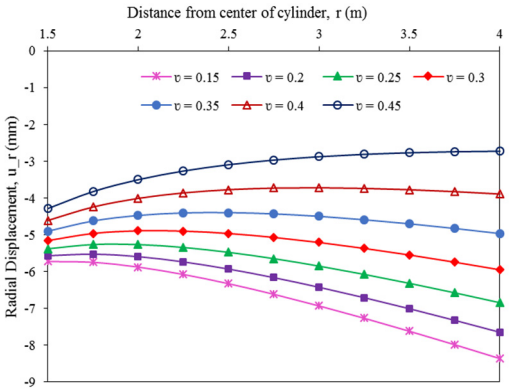

Fig. 9 Variations of radial displacement with respect to the distance from the center of the cylinder for modulus of elasticity of 40 Gpa and different values of Poisson's ratio from 0.15 to 0.45 in the single layer

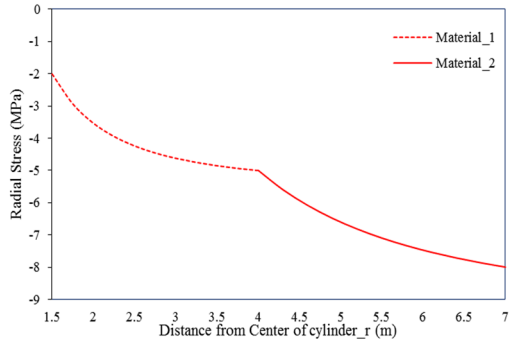

Fig. 10 Radial stress diagrams in materials (1) and (2), respectively, when material (1) is the internal material and material (2) is the external material

the radial and tangential stresses, respectively. As can be seen from Figs. 6 and 7, with the increase of internal pressure, the values of radial and tangential stresses increase and decrease, respectively, in the stone cylinder. In addition, when the internal uniform compressive load value is equal to the external uniform compressive load value (P=Q=8 Mpa), the values of radial and tangential stresses do not depend on the radial distance from the center of the cylinder, and during the path from the inner radius to the outer radius of the cylinder, their values are constant and equal applied pressure loads are (8 Mpa).

Fig. 8 shows the effect of modulus of elasticity on radial displacement. As can be seen, with the increase of the elasticity modulus, the radial displacement decreases non-linearly.

Fig. 9 illustrates the behavior of radial displacement as a function of the distance from the center of the cylinder, comparing different Poisson's ratios in the single-layer model with an elastic modulus of 40 GPa. As can be seen, with the increase of Poisson's ratio, the changes of radial locations decrease non-linearly.

2.5 Diagrams of the 2-layer model

Figs. 10 and 11 illustrate the radial and tangential stress diagrams for materials (1) and (2), respectively, when

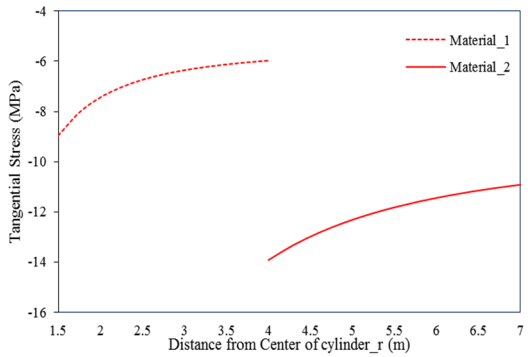

Fig. 11 Tangential stress diagrams in materials (1) and (2), respectively, when material (1) is the internal material and material (2) is the external material

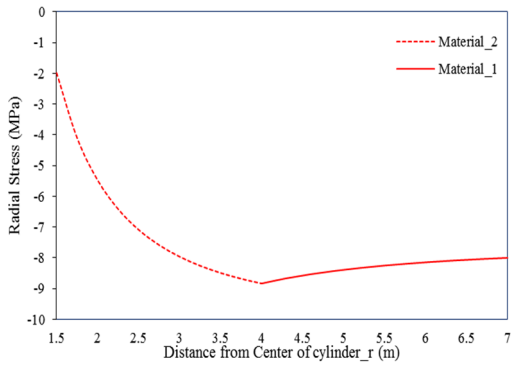

Fig. 12 Radial stress diagrams in materials (1) and (2), respectively, when material (2) is the internal material and material (1) is the external material

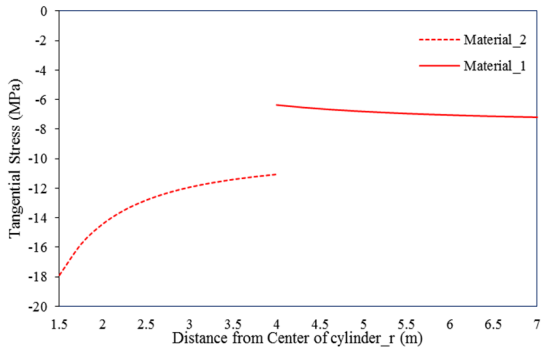

Fig. 13 Tangential stress diagrams in materials (1) and (2), respectively, when material (2) is the internal material and material (1) is the external material

material (1) is the internal component and material (2) is the external component. In contrast, Figs. 12 and 13 present similar diagrams for the case where material (2) is the internal component and material (1) is the external component of the composite system.

Figs. 14 and 15 show radial and tangential stress diagrams in materials (1) and (3), respectively, when material (1) is the internal material and material (3) is the external material. Figs. 16 and 17 also show the mentioned diagrams, unlike the previous case, when material (3) is the internal material and material (1), the external material of the composite system.

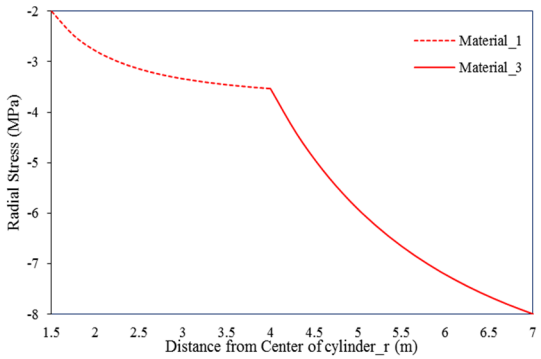

Fig. 14 Radial and tangential stress diagrams in materials (1) and (3), respectively, when material (1) is the internal material and material (3) is the external material

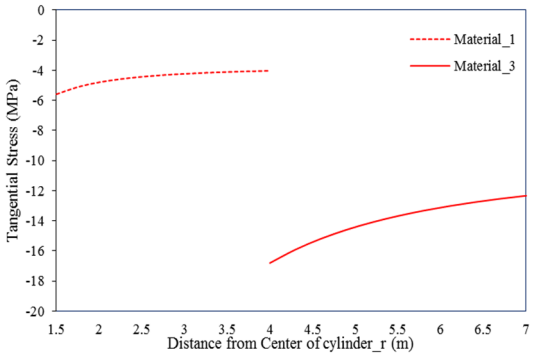

Fig. 15 Tangential stress diagrams in materials (1) and (3), respectively, when material (1) is the internal material and material (3) is the external material

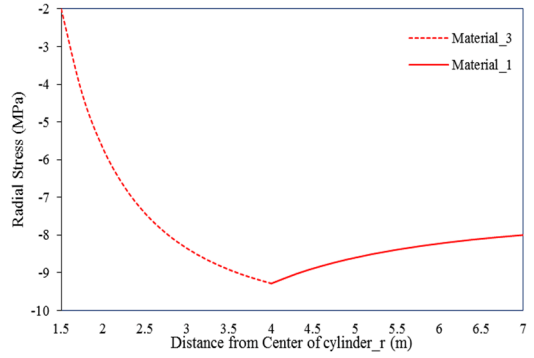

Fig. 16 Radial and tangential stress diagrams in materials (1) and (3), respectively, when material (3) is the internal material and material (1) is the external material

Figs. 18 and 19 display the radial and tangential stress diagrams for materials (2) and (3), respectively, with material (2) acting as the internal material and material (3) as the external material. In contrast, Figs. 20 and 21 show the same stress diagrams when material (3) is the internal material and material (2) is the external material of the composite system.

Fig. 22 illustrates the radial stress diagram for two different scenarios: a) when the inner cylinder is constructed from material 1 and the outer cylinder is made of material 2, and b) when the inner cylinder is made of material 1 and the outer cylinder is composed of material 3.

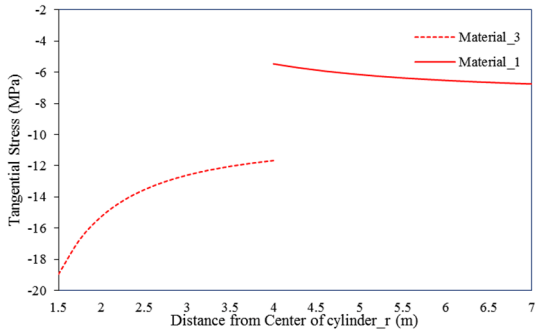

Fig. 17 Tangential stress diagrams in materials (1) and (3), respectively, when material (3) is the internal material and material (1) is the external material

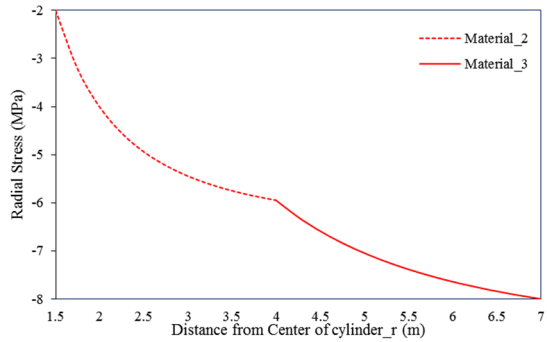

Fig. 18 Radial stress diagrams in materials (2) and (3), respectively, when material (2) is the internal material and material (3) is the external material

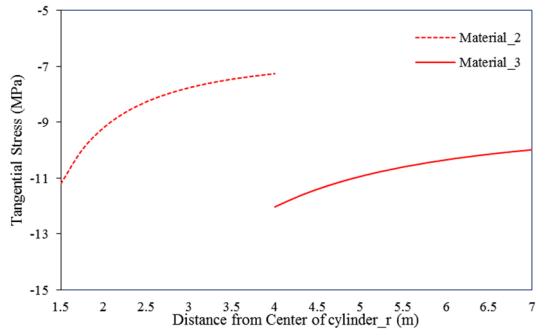

Fig. 19 Tangential stress diagrams in materials (2) and (3), respectively, when material (2) is the internal material and material (3) is the external material

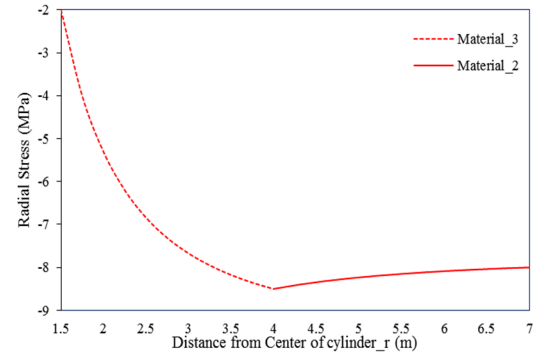

Fig. 20 radial stress diagrams in materials (2) and (3), respectively, when material (3) is the internal material and material (2) is the external material

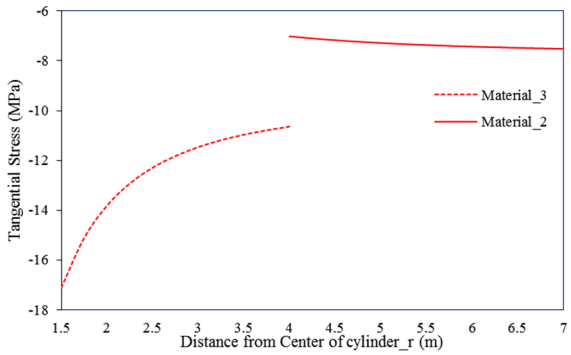

Fig. 21 Tangential stress diagrams in materials (2) and (3), respectively, when material (3) is the internal material and material (2) is the external material

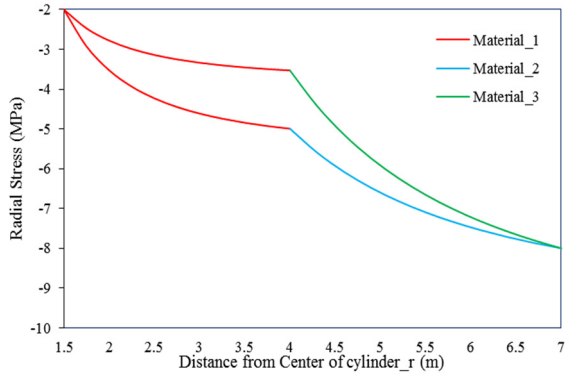

Fig. 22 Radial stress diagram in 2 cases: a) the inner cylinder is made of material 1 and the outer cylinder is made of material 2 and b) the inner cylinder is made of material 1 and the outer cylinder is made of material 3

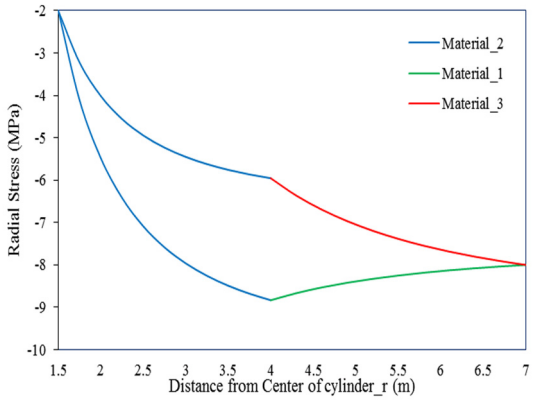

Fig. 23 Radial stress diagram in 2 cases: a) the inner cylinder is made of material 2 and the outer cylinder is made of material 1 and b) the inner cylinder is made of material 2 and the outer cylinder is made of material 3

Fig. 23 illustrates the radial stress diagram for two scenarios: a) when the inner cylinder is composed of material 2 and the outer cylinder is made of material 1, and b) when the inner cylinder remains material 2 while the outer cylinder is made of material 3.

Fig. 24 illustrates the radial stress diagram for two cases: a) when the inner cylinder is composed of material 3 and the outer cylinder is composed of material 1, and b)

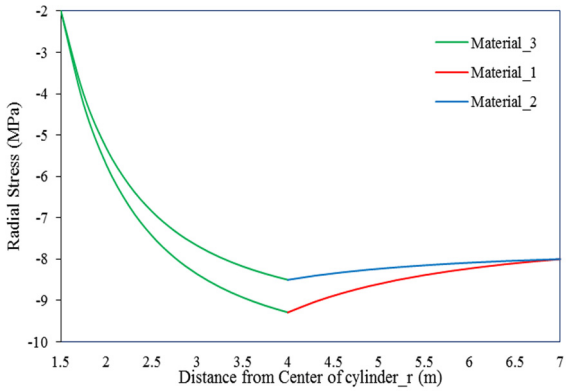

Fig. 24 radial stress diagram in 2 cases: a) the inner cylinder is made of material 3 and the outer cylinder is made of material 1 and b) the inner cylinder is made of material 3 and the outer cylinder is made of material 2

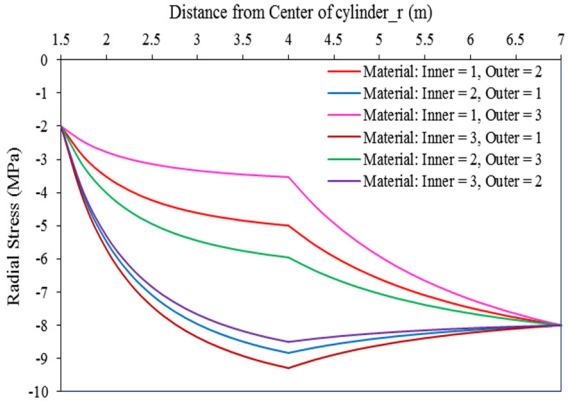

Fig. 25 Radial stress changes for 6 positions of 3 different materials in the 2-layer model (inner and outer cylinder)

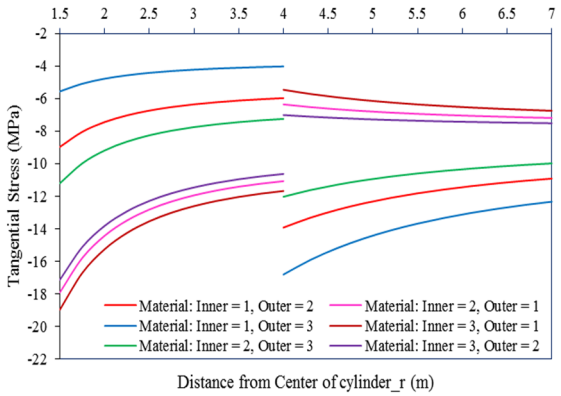

Fig. 26 Changes in tangential stress for 6 positions of 3 different materials in the 2-layer model (inner and outer cylinder)

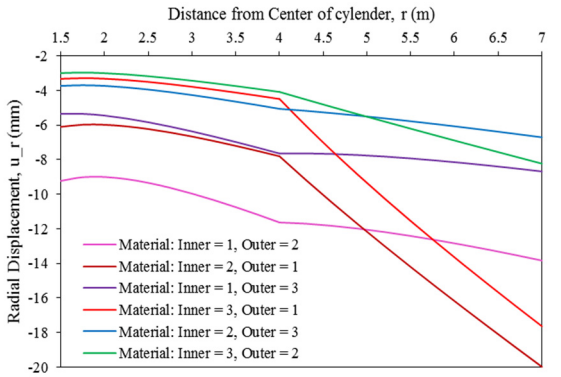

Fig. 27 Radial displacement changes in 6 positions of 3 different materials in the two-layer model

when the inner cylinder is made of material 3 and the outer cylinder is made of material 2.

Fig. 25 shows the different states (6 states) of the placement of composite materials relative to each other in the 2-layer model and their effect on the radial stress field. In all cases, moving away from the inner border of the inner cylinder and moving towards the interface between the two cylinders, the radial stresses increase. However, this increasing trend in radial stresses in the inner cylinder is different depending on the modulus of elasticity of the inner cylinder. As can be seen, when the inner cylinder material has a lower modulus of elasticity than the outer cylinder, compared to the case where the inner cylinder has a higher modulus of elasticity than the outer cylinder, the increasing trend in radial stresses is lower. Also, when the material forming the inner cylinder has a lower modulus of elasticity than the outer cylinder, the radial stress at the interface between the two cylinders is less than the uniform compressive load (Q) and in such a case, the radial stress increases when passing through the interface between the two materials. It is maintained up to the outer border of the outer cylinder. In contrast to the previous case, when the material of the inner cylinder has a higher modulus of elasticity than that of the outer cylinder, the radial stress at the interface between the two cylinders exceeds the uniform compressive load (Q). Consequently, as we move from the inner material to the outer material, there is a downward trend in radial stress until we reach the outer edge of the outer cylinder.

Fig. 26 shows the diagrams related to the tangential stress field in 6 positions of 3 different materials relative to each other in the 2-layer model. As can be seen, the larger the ratio of the modulus of elasticity of the inner cylinder to the outer cylinder, the greater the tangential stress values in the inner cylinder and the smaller in the outer cylinder. In this study, we consider three materials with elasticity moduli: E1 = 12 GPa, E2 = 40 GPa, and E3 = 80 GPa. The maximum tangential stress in the inner cylinder and the minimum tangential stress in the outer cylinder are related to the modulus ratio (12/80). This scenario occurs when the inner layer is made from material 3 and the outer layer is made from material 1, as illustrated in the brown diagram. Another point that can be seen from Fig. 26 is that the tangential stresses are not continuous at the junction of two cylinders.

The diagrams in Fig. 27 illustrate the radial displacement field across six different states of material arrangement in the 2-layer model. It can be observed that the trend of changes in radial displacement consistently increases from the inner border of the inner cylinder to the outer border of the outer cylinder.

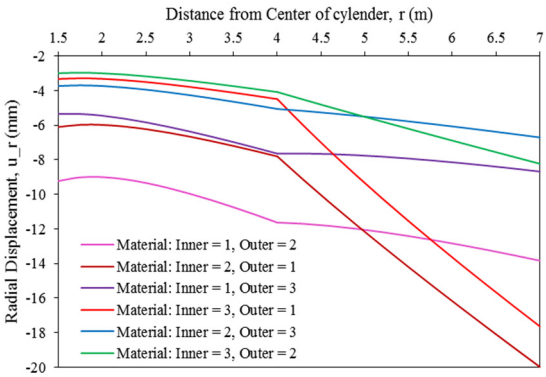

Fig. 27 Radial displacement changes in 6 positions of 3 different materials in the two-layer model

2.6 Diagrams of the 3-layer model

Fig. 28 shows the diagram of radial stress in 6 positions of 3 different materials relative to each other in the 3-layer model. As can be seen from this figure, the radial stress always increases in the inner cylinder as the inner border moves away and approaches the interface between the inner and middle cylinders. By passing through the interface of the inner and middle cylinder and approaching the interface of the middle and outer cylinder, if the modulus of elasticity of the middle cylinder is lower than that of the inner cylinder, the amount of radial stress will gradually decrease. But when the modulus of elasticity of the middle cylinder is higher than that of the inner cylinder, the increasing trend in the amount of radial stress in the middle layer is maintained. Upon entering the outer layer, when the modulus of elasticity of this layer is lower than that of the middle layer, the radial stress value gradually decreases until it reaches the uniform compressive load value of 8 MPa at the outer border of the outer cylinder. On the other hand, if the modulus of elasticity of this layer is greater than that of the middle layer, the radial stress value will gradually increase until it reaches the uniform compressive load value of 8 MPa at the outer border of the outer cylinder.

Fig. 29 shows the diagrams of tangential stress in 6 different positions of materials relative to each other. In all cases of placement of materials relative to each other in the 3-layer model, the amount of tangential stress in the inner layer is always gradually reduced by moving away from the inner border of the inner cylinder and approaching the interface between the inner and middle cylinders. In the middle and outer layers, respectively, if the modulus of elasticity of the middle layer is greater than that of the inner layer and the modulus of elasticity of the outer layer is greater than that of the middle layer, the tangential stress will continue to decrease by moving away from the interface between the inner and the middle cylinder as well as the middle and the outer cylinder has it. On the other hand, if the modulus of elasticity of the middle layer is lower than that of the inner layer and the modulus of elasticity of the outer layer is also lower than that of the middle layer, the tangential stress of the process increases with a slight slope as you move away from the interface of the inner and middle cylinder as well as the middle and outer cylinder. It can also be seen from Fig. 29 that the value of tangential stress is not continuous at the interface of two materials, and a great change occurs in its value upon entering another material. Another point that can be understood from this diagram is that in a specific position of the materials relative to each other, the greater the modulus of elasticity of the materials that make up the layers, the greater the value of the tangential stress in that layer.

Fig. 30 illustrates the radial deformation in six different positions of materials 1, 2, and 3 relatives to each other. From this figure, it can be seen that, in general, regardless of how the materials are placed in relation to each other, radial displacements always increase by moving away from the inner cylinder's outer boundary and approaching the outer cylinder's outer boundary. Also, the minimum radial displacement occurs at the inner cylinder's circumferential boundary, and the maximum radial displacement occurs at the outer cylinder's outer boundary. In this diagram, the negative value of the radial displacement indicates the compression of cylindrical layers. The same behavior is also observed in model 2. Another point that can be understood from this diagram in Fig. 30 is that in a specific position of the materials relative to each other, the smaller the modulus of elasticity of the materials that make up a layer is, the amount of radial displacement increases with a steeper slope and a faster trend. Also, radial displacements are continuous at the interface of materials.

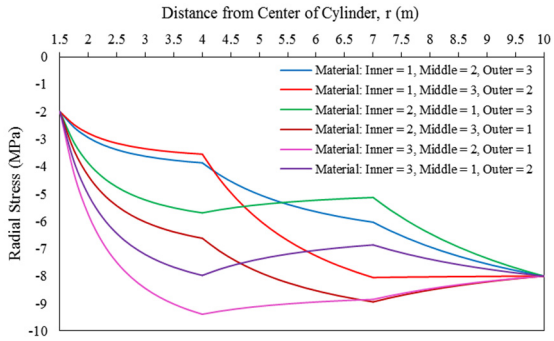

Fig. 28 Radial stress changes in 6 positions of 3 different materials in the 3-layer model

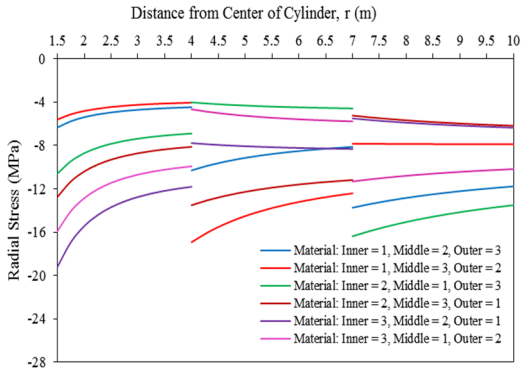

Fig. 29 Changes in tangential stress in 6 positions of 3 different materials in the 3-layer model

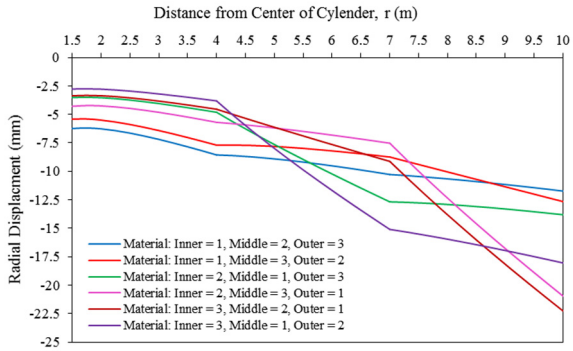

Fig. 30 Radial displacement changes in 6 positions of 3 different materials relative to each other in the 3-layer model

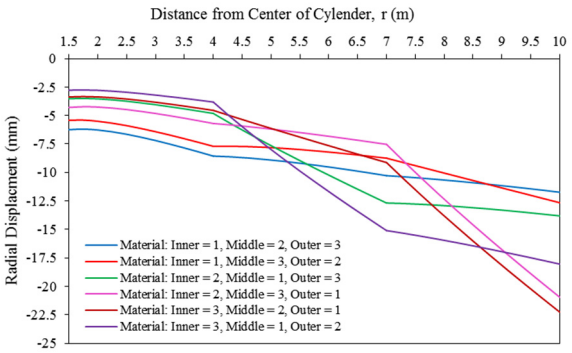

Fig. 31 Variations of the critical radius of failure in relation to the compressive loads applied to the inner border of the cylinder for different values of the uniaxial compressive strength of the material

3. Analysis of failure in cylindrical samples

In order to investigate the failure mechanism in single-layer, 2-layer and 3-layer cylindrical specimens, the Mohr-Coulomb failure criterion is used here according to Eq. (32)

$$\sigma_1 = \sigma_c + \sigma_3 \left(\frac{1+\sin\phi}{1-\sin\phi} \right) \tag{32}$$

In the above relationship, ϕ the angle of internal friction, σ_c the uniaxial compressive strength of the cylindrical rock sample, $\sigma_3$the minimum main stress applied to the rock sample and $\sigma_1$the maximum main stress. Since the shear stress applied to the cylindrical samples is equal to zero, so the tangential and radial stresses play the role of the main stresses (minimum and maximum) in this problem for the Mohr-Coulomb selective failure criterion. In the following, we obtain the range of fracture caused by radial and tangential applied stresses to cylindrical samples in 3 modes of single-layer, two-layer and three-layer models.

3.1 Determining the range of failure in the single-layer model

In the case of a single layer, according to the obtained radial and tangential stress diagrams, the radial stress values for 3 materials with different characteristics presented in table (1) are the same and do not depend on the properties of the materials. Also, the values of the tangential stresses in the single-layer state for 3 different materials are independent of the properties of the materials and are equal. On the other hand, the amount of radial stress in 3 materials (which are equal) in this case is less than the values of tangential stress. Therefore, in the Mohr-Coulomb criterion, the tangential stress is considered as the maximum principal stress (σ_1) and the radial stress is considered as the minimum principal stress (σ_3). Therefore, the condition of failure in rock samples in the single-layer model according to the Mohr-Coulomb criterion for 3 materials with uniaxial compressive strength and different internal friction angle can be represented according to Eq. (33)

$$\sigma_\theta \geq \sigma_{Ci} + \sigma_r \left(\frac{1+\sin\phi_i}{1-\sin\phi_i} \right) \quad ; \quad i = 1,2,3 \tag{33}$$

On the other hand, the values of radial and tangential stresses are negative according to the graphs drawn for single-layer, 2-layer and 3-layer models. The negativity of these values indicates that the aforementioned stresses are compressive. Therefore, in relation 33, in order to agree with the sign of the compressive strength of the material, we should insert the relation of radial and tangential stresses, i.e.,

$\sigma_r = -\frac{A}{r_i^2} - B$ and $\sigma_\theta = \frac{A}{r_i^2} - B$ in relation 33. As a result, the critical fracture radius (r_c) of the samples for the single-layer model can be expressed according to Eq. (34)

$$\left(\frac{A}{r^2} - B \right) \geq \sigma_C + \left(-\frac{A}{r^2} - B \right) \left(\frac{1+\sin\phi}{1-\sin\phi} \right) \Rightarrow$$
$$r_c \leq \sqrt{\frac{2A}{\sigma_C (1-\sin\phi) - 2\sin\phi B}} \tag{34}$$

In the above relationship, parameters A and B are equal to

$$\begin{cases} A = \dfrac{(Q-P) R_0^{\,2} R_1^{\,2}}{\left(R_1^{\,2} - R_0^{\,2} \right)} \\ B = \dfrac{P R_0^{\,2} - Q R_1^{\,2}}{\left(R_1^{\,2} - R_0^{\,2} \right)} \end{cases} \tag{35}$$

By placing the values of the required parameters related to 3 different materials according to Table 1 in relation (34), the value of the critical radius for materials 1, 2 and 3 is obtained as follows:

$r_{C1} \leq 1.695m$; $r_{C2} \leq 1.533m$; $r_{C3} \leq 1.447m$

Considering that the critical radius obtained in material 3 is lower than the inner radius of the cylinder in the single-layer model, therefore, failure in material 3 with a compressive strength of 9 MPa does not occur under uniform internal loading system of 2 MPa and external 8 MPa. However, failure occurs in materials 1 and 2 with compressive strengths of 2 MPa and 6 MPa, respectively, under the mentioned loading system. In materials 1 and 2, the fracture occurs at radial distances of 1.5 m to 1.695 m (195 mm long) and 1.5 m to 1.533 m (33 mm long) from the center of the cylinder, respectively. Another point is that

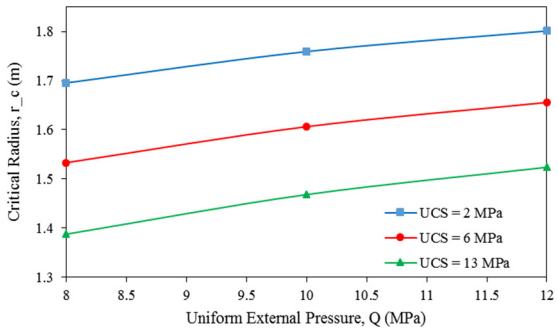

Fig. 32 Variations of the critical radius of failure in relation to the compressive loads applied to the external border of the cylinder for different values of the uniaxial compressive strength of the material

the extension of failure in cylinders is from the inner border to the outer border. In addition, the radius of the fracture zone of the cylinders is strongly influenced by the uniform compressive loads applied to the inner and outer borders of the cylinders. As can be seen from Figs. 31 and 32, the critical fracture radius of the cylinders has a direct relationship with the compressive load applied to the outer border of the cylinder and an inverse relationship with the compressive load applied to the inner border of the cylinders. In other words, by increasing the compressive load applied to the outer border of the cylinder or by decreasing the compressive load applied to the inner border of the cylinder, the critical radius of failure increases. On the other hand, by reducing the compressive load applied to the outer border of the cylinder or by increasing the compressive load applied to the inner border of the cylinder, the critical radius of failure decreases.

3.2 Determining the range of failure in the 2-layer model

When two cylindrical layers are considered, it has been observed that the tangential stress induced in the inner layer consistently exceeds that of the radial stress, as illustrated in Figs. 25 and 26. Therefore, in the inner layer, the maximum main stress is tangential and the minimum stress is radial. The minimum principal stress in the Mohr-Coulomb relationship is considered to determine the critical radius of fracture in this layer. If the elasticity modulus of the outer layer is greater than that of the inner layer, the tangential and radial stresses are the maximum and minimum principal stresses, respectively, based on the Mohr-Coulomb failure criteria. On the other hand, if the outer layer has a modulus of elasticity lower than that of the inner one, the tangential stress is the minimum stress, and the radial stress is the maximum stress in the Mohr-Coulomb criterion of failure. When evaluating the maximum tangential stress and minimum radial stress, three cases can be examined: i) using material 1 for the inner layer and material 2 for the outer layer; ii) using material 3 for the outer layer and material 1 for the inner layer; iii) using material 2 for the inner layer and material 3 for the outer layer. The critical failure radius can be obtained using Eq. (34) as already given for the case of a single-layer sample. For the case that the elasticity modulus of outer layer is lower than that of the inner one, also three cases can be considered as: i) material 1 for the outer layer and material 2 for the inner one; ii) material 3 for the outer layer and material 1 for the inner one; iii) material 3 for the inner layer and material 1 for the outer one. The tangential stress in the outer layer is smaller than the radial stress, and therefore, taking into account the

$$\begin{cases}\sigma_1=-\sigma_r=-\left(\dfrac{A^{(O)}}{r_c^{\,2}}+B^{(O)}\right)\\ \sigma_3=-\sigma_\theta=-\left(-\dfrac{A^{(O)}}{r_c^{\,2}}+B^{(O)}\right)\end{cases}$$ in Mohr-Coulomb

relationship, the critical radius of failure in the outer layer can be determined by Eq. (36)

$$\begin{aligned}&\sigma_r\ge\sigma_{Co}+\sigma_\theta\left(\frac{1+\sin\phi_o}{1-\sin\phi_o}\right)\\&\Rightarrow-\left(\frac{A^{(O)}}{r_c^{\,2}}+B^{(O)}\right)\ge\sigma_{Co}\\&-\left(-\frac{A^{(O)}}{r_c^{\,2}}+B^{(O)}\right)\left(\frac{1+\sin\phi_o}{1-\sin\phi_o}\right)\\&\Rightarrow r_c^{\,O}\ge\sqrt{\frac{2A^{(O)}}{2\sin\phi_o B^{(O)}-\sigma_{Co}\left(1-\sin\phi_o\right)}}\end{aligned}\tag{36}$$

So, we have 6 different modes

- The inner layer of type 1 material and the outer layer of type 2 material, in this case the critical radii are respectively equal to $\begin{cases}r_c^{\,1}\le 1.49m\\ r_c^{\,2}\le 3.91m\end{cases}$:
- The inner layer is from material 1 and the outer layer is from material 3. In this case, the critical radii are equal to: $\begin{cases}r_c^{\,1}\le 1.25m\\ r_c^{\,3}\le 3.44m\end{cases}$
- The inner layer is made of material 2 and the outer layer is made of material 3. In this case, the critical radii are equal to: $\begin{cases}r_c^{\,2}\le 1.4m\\ r_c^{\,3}\le 3.54m\end{cases}$
- The inner layer is made of material 2 and the outer layer is made of material 1. In this case, the critical radii are equal to: $\begin{cases}r_c^{\,2}\le 1.56m\\ r_c^{\,1}\ge 2.05m\end{cases}$
- The inner layer is made of material 3 and the outer layer is made of material 1. In this case, the critical radii are equal to: $\begin{cases}r_c^{\,3}\le 1.44m\\ r_c^{\,1}\ge 2.59m\end{cases}$
- The inner layer is made of material 3 and the outer layer is made of material 2. In this case, the critical radii are equal to: $\begin{cases}r_c^{\,3}\le 1.41m\\ r_c^{\,2}\ge 1.41m\end{cases}$

In none of the six cases discussed did the critical radius for the failure of the external cylinder fall below the internal radius of the external cylinder. As a result, failure does not

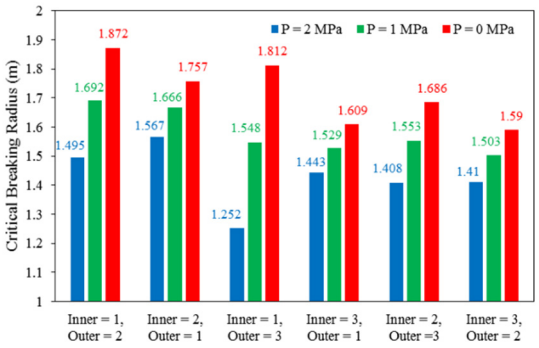

Fig. 33 The effect of internal uniform compressive load changes on the critical fracture radius of the internal cylinder in 6 positions of materials relative to each other in the 2-layer model for Q = 8 MPa

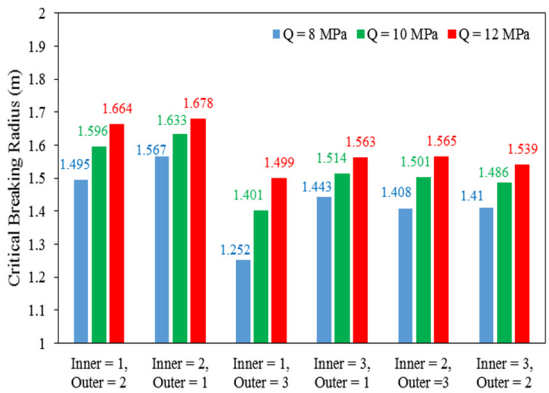

Fig. 34 The effect of external uniform compressive load changes on the critical fracture radius of the inner cylinder in 6 positions of materials relative to each other in the 2-layer model for P = 2 MPa

occur in the external cylindrical rock layers. For the internal cylinders, failure only occurs when the material is of type 2 and the material of the external cylinder is type 1, given the corresponding loading conditions. In this specific scenario, failure occurs at a radial distance of 1.5 m to 1.56 m from the center of the cylinders, which is 60 mm from the inner wall. In the other five cases, no failure is reported in the inner cylinders.

When the internal uniform pressure is reduced from 2 MPa to 1 MPa, failure still does not occur in the outer cylinders. However, under these conditions, failure does occur in the inner cylinders across all six configurations of materials. The critical radius of failure for the inner cylinders in these cases is as follows:

1. When the inner layer is made of material 1 and the outer layer is made of material 2, the critical radius of internal cylinder fracture is 192 mm.
2. When the inner layer is made of material 1 and the outer layer is made of material 3, the critical radius of internal cylinder fracture is 48 mm.
3. When the inner layer is made of material 2 and the outer layer is made of material 3, the critical radius of internal cylinder fracture is 53 mm.
4. When the inner layer is made of material 2 and the outer layer is made of material 1, the critical radius of internal cylinder fracture is 166 mm.
5. When the inner layer is made of material 3 and the outer layer is made of material 1, the critical radius of internal cylinder fracture is 29 mm.
6. When the inner layer is made of material 3 and the outer layer is made of material 2, the critical radius of internal cylinder fracture is 3 mm.

Figs. 33 and 34 illustrate the effects of changes in internal and external uniform compressive loads on the critical fracture radius of the internal cylinder across the six material configurations in the two-layer model. According to these figures, an increase in uniform external pressure (Q), similar to a decrease in internal uniform pressure (P), causes the critical radius of failure in the inner cylinder to increase. Thus, in this two-layer state, just as in a single-layer state, failure occurs in all internal cylinders when either the external uniform pressure increases or the internal uniform pressure decreases, since the critical radius of failure exceeds the radius of the internal cylinder. However, failure in the outer cylinders does not occur under any circumstances.

3.3 Determining the range of failure in the 3-layer model

In the 3-layer model, in all 6 positions of the materials relative to each other, in the inner layer, the value of tangential stresses is greater than the radial stresses, so in the Mohr-Coulomb criterion, the tangential stress is considered as the maximum principal stress and the radial stress as the minimum principal stress (Note that relative values of these stresses are placed in the Mohr-Coulomb relation). Therefore, in this case, Eq. (34) can be used to determine the critical radius of fracture in the inner layer, similar to the single-layer and 2-layer cases. For the middle layers, if the modulus of elasticity is higher than the inner layer, the value of the critical radius of fracture can be determined from Eq. (34). However, if its modulus of elasticity is lower than the modulus of elasticity of the inner layer, Eq. (36) can be used to determine the critical radius of fracture. In the outer layer, if its modulus of elasticity is higher than the middle layer, we use Eq. (34) to determine the critical radius of failure. On the other hand, if the elastic modulus of the outer layer is less than the elastic modulus of the middle layer, the critical radius of failure is obtained from Eq. (36). By substituting the required parameter values from Table 1 and considering internal and external uniform pressure loads of 2 MPa and 8 MPa, respectively, into Eqs. (34) and (36), it is concluded that no fractures occur in the inner, middle, or outer layers of the three-layer model under any of the six configurations of material placement, according to the Mohr-Coulomb criterion. Similarly, to the 2-layer model, in the 3-layer model, with the decrease of internal uniform pressure or the increase of external uniform pressure, the critical radius of failure of the cylindrical layers also increases, and the failure of the inner cylinders gradually occurs depending on their uniaxial compressive strength. In general, the lower the uniaxial compressive strength of the inner layer, the greater the

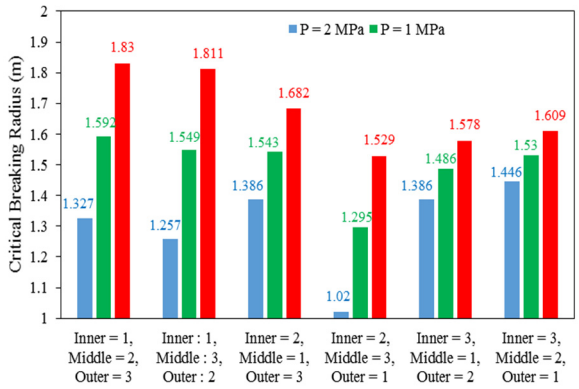

Fig. 35 The effect of internal uniform compressive load changes on the critical fracture radius of the internal cylinder in 6 positions of materials relative to each other in the 3-layer model for Q = 8 MPa

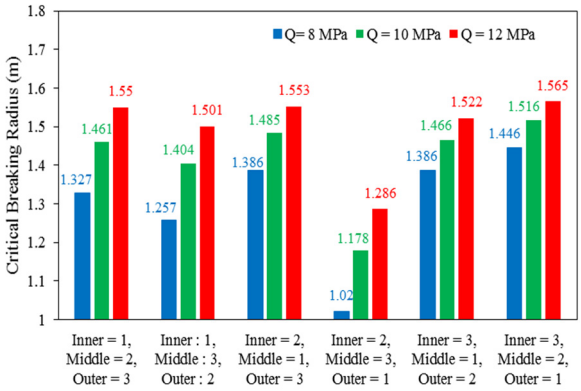

Fig. 36 The effect of external uniform compressive load changes on the critical radius of internal cylinder fracture in 6 positions of materials relative to each other in the 3-layer model for P = 2 MPa

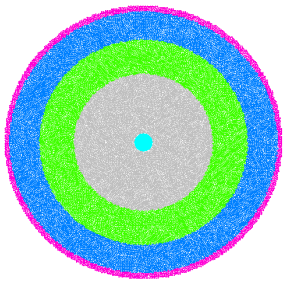

Fig. 37 Three circle layers with different mechanical properties, i.e., soft rock (blue color), medium strength rock (gray color) and hard rock (green color)

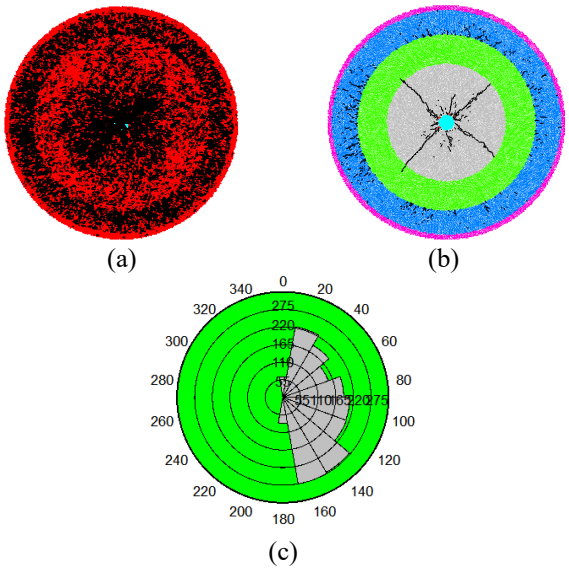

Fig. 38 (a) Contact force distribution in numerical model after the crack growth, (b) crack growth pattern and (c) rose diagram of crack growth

critical radius of failure. This phenomenon is illustrated in Figs. 35 and 36, which demonstrate the impact of internal and external uniform pressures on the critical radius of fracture in six positions of cylinders made from three different types of materials. In these figures, when the critical radius of fracture exceeds the inner radius of the inner cylinder (1.5 m), fracture occurs within the inner cylinder according to the Mohr-Coulomb criterion. Specifically, the fracture extends from the inner wall of the cylinder by an amount equal to the difference between the critical radius and the inner radius of the inner cylinder.

4. The verification of analytical method

Particle flow code in two dimensions was used for the verification of the analytical method. A disc model with a diameter of 2500 mm was prepared (Fig. 37). This model was consisted of three circle layers with different mechanical properties, i.e., soft rock with a uniaxial strength of 2 MPa (blue color in Fig. 37), medium strength rock with uniaxial strength of 6 MPa (gray color in Fig. 1) and hard rock with uniaxial strength of 13 MPa (green color in Fig. 37). These layers were pressurized by central pressure hole (low blue color in Fig. 37). Three internal pressures were applied into the model, i.e., 0 MPa, 1 MPa and 2 MPa. These layers were surrounded by an external circle layer (purple color in Fig. 37). Three different confining pressures were applied by movement of the external layer toward the other three layers, i.e., 8 MPa, 10 MPa, and 12 MPa. The tests were finished when internal pressure led to the failure of the model. Micro-parameter calibration was used to adjust macro-properties. Initially, through trial and error, the Young's modulus of both the flat joint model and the particles was modified to calibrate the overall Young's modulus. Following that, the adhesion and tensile strength were altered simultaneously in order to calibrate the compressive strength and the large-scale Brazilian tensile strength.

Fig. 38(a) shows the contact force distribution in the numerical model after the crack growth. The red line and black colors are representative of tensile force and compressive force, respectively. The tensile forces were distributed in the middle layer, while compressive forces were distributed in the first and third layers. This shows that the middle layer, that have high tensile strength, is stable during the test, while the two other layers with low and

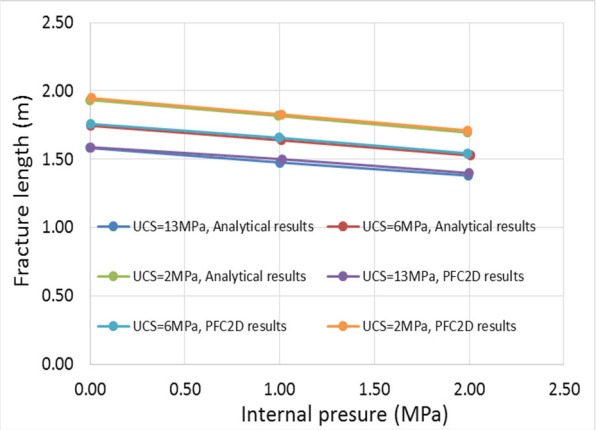

Fig. 39 Variations of fracture length versus the internal pressure for different values of the uniaxial compressive strength of the material

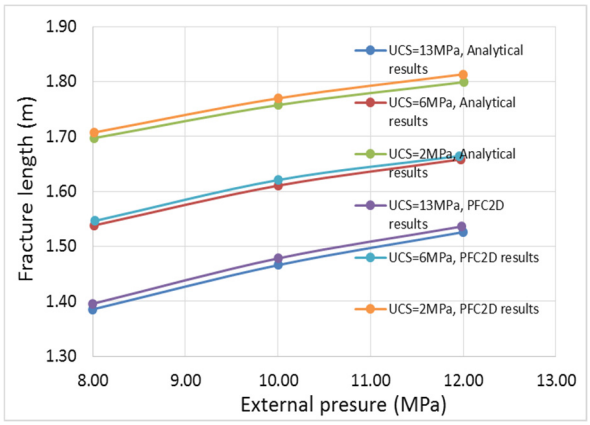

Fig. 40 Variations of fracture length versus the external pressure for different values of the uniaxial compressive strength of the material

medium tensile strength will be broken. Fig. 38(b) shows crack propagation in the numerical model after the crack growth. The black line and red lines are representative of tensile crack and shear crack, respectively. Also, Fig. 38(c) shows the rose diagram of crack growth. Four major tensile fracture sets were developed in the medium-strength model, while a large number of small cracks were developed in weak rock. The middle layer that has high tensile strength was stable. This shows that the middle hard layer can transfer the internal force to the weak rock after crack propagation in the first layer. This leads to small crack growth in soft rock. The dip angles of large fracture sets related to the vertical axis were 45 degrees.

Determining the range of failure in the single-layer model

Figs. 39 and 40 show the variation of fracture length based on internal pressure and external pressure in the single-layer model, respectively. These results were allocated to both the analytical method and the numerical simulation.

The critical fracture radius of the cylinders has a direct relationship with the compressive load applied to the outer border of the cylinder and an inverse relationship with the compressive load applied to the inner border of the cylinders. In other words, by increasing the compressive load applied to the outer border of the cylinder or by decreasing the compressive load applied to the inner border of the cylinder, the critical radius of failure increases. On the other hand, by reducing the compressive load applied to the outer border of the cylinder or by increasing the compressive load applied to the inner border of the cylinder, the critical radius of failure decreases. Both the analytical method and numerical simulation have similar results. As the angle of the layer increases, a larger portion of the crack moves through the first layer. If this layer is brittle, the crack grows and spreads quickly and instantaneously. However, if the layer is deformable, the growth of the hydraulic crack is delayed. When the angle of the layer is small, the hydraulic crack can pass through most of the previous layers, exhibiting either delayed or progressive behavior, depending on the types of layers involved.

The thickness of the layer is directly related to how quickly the crack propagates. With an increase in the thickness of a brittle layer, the crack growth occurs rapidly. In contrast, as the thickness of a deformable layer increases, the crack growth is slower.

Geophysical methods can identify layers deep within the earth. If these layers are arranged so that brittle and resistant layers are facing the well, the injection pressure needs to be sufficient to overcome both the tensile strength of these layers and the confining pressure. However, if ductile layers are encountered, the energy required to create a hydraulic fracture increases significantly. This occurs because the water pressure applied is primarily used to deform the rock rather than to propagate and expand the crack.

5. Conclusions

An analytical solution was employed to examine how the mechanical properties of the bedding plane influence hydraulic fracture growth. The study aimed to investigate the effects of the number of bedding layers, the mechanical properties of these layers, internal pressure, and confining pressure on radial displacement, radial stress, tangential stress, and the critical radius of failure concerning crack propagation mechanisms, crack growth paths, and the interactions of the hydraulic fracture network with bedding planes and natural fractures. The following main conclusions were drawn:

- Effects of bedding planes' geometries on the crack propagation mechanism of hydraulic fractures are considered.
- The values of radial stresses increase and constitute the maximum principal stress in the specimens as the internal pressure increases. On the other hand, the values of tangential stresses decrease when the internal pressure increases in the sample,
- When the uniform internal and external compressive loads on the cored disc specimen are the same, the radial and tangential stresses do not change with changing the radial distance from the center of the cylindrical specimen.

- The propagation of hydraulic fracture is enhanced as the elastic modulus of the layer decreases while its strength increases. The shear failure in the bedding layers is enhanced, and the growth of hydraulic fracture increases as the strength of the bedding layer decreases.
- The shear strength decreases when its cohesion and its internal friction angle decrease, and therefore, the propagation of hydraulic fracturing is enhanced while crossing the bedding layers in the gas shale formations.

Acknowledgments

This work was supported by National Natural Science Foundation of China (No. 52479100), National Foreign Experts Program of China (No. S20240157 and No. H20240271), and Outstanding Foreign Scientist Studio of Henan Province (No. GZS2025015).

References

Adıyaman, G., Birinci, A., Öner, E. and Yaylacı, M. (2016), "A receding contact problem between a functionally graded layer and two homogeneous quarter planes", *Acta Mech*., **227**, 1753-1766.

Ajamzadeh, M.R., Sarfarazi, V., Haeri, H. and Dehghani, H. (2018), "The effect of micro parameters of PFC software on the model calibration", *Smart Struct. Syst*., **22**(6), 643-662. https://doi.org/10.12989/sss.2018.22.6.643.

Akbas, S. (2016), "Analytical solutions for static bending of edge cracked micro beams". *Struct. Eng. Mech*., **59**(3), 66-78. https://doi.org/10.12989/sem.2016.59.3.579.

Banjara, N.K., Sasmal, S. and Srinivas, V. (2019), "Damage progression study in fibre reinforced concrete using acoustic emission technique", *Smart Struct. Syst*., **23**(2), 173-184. https://doi.org/10.12989/sss.2019.23.2.173.

Cui, Z. and Han, W. (2018), "In situ scanning electron microscope (SEM) observations of damage and crack growth of shale", *Microsc. Microanal*., **24**, 107-115. https://doi.org/10.1017/S1431927618000211.

Daneshy, A.A. (1978), "Hydraulic fracture propagation in layered formations", *Soc. Pet. Eng. J*., **18**, 33-41. https://doi.org/10.2118/6088-PA.

Fu, W., Savitski, A.A., Damjanac, B. and Bunger, A.P. (2019), "Three-dimensional lattice simulation of hydraulic fracture interaction with natural fractures", *Comput. Geotech*., **107**, 214-234. https://doi.org/10.1016/j.compgeo.2018.11.023.

Golewski, G.L. (2019), "The influence of microcrack width on the mechanical parameters in concrete with the addition of fly ash: Consideration of technological and ecological benefits", *Constr. Build. Mater.*, **197**, 849-861. https://doi.org/10.1016/j.conbuildmat.2018.08.157.

Golewski, G.L. (2022), "An extensive investigations on fracture parameters of concretes based on quaternary binders (QBC) by means of the DIC technique", *Constr. Build. Mater*., **351**, 128823. https://doi.org/10.1016/j.conbuildmat.2022.128823.

Golewski, G.L. (2023), "Combined effect of coal fly ash (CFA) and nanosilica (nS) on the strength parameters and microstructural properties of eco-friendly concrete", *Energies*, **16**(1), 452. https://doi.org/10.3390/en16010452.

Gong, T., Xia, B., Liu, L., Peng, Z. and Gao, Y. (2019), "Propagation of hydraulic fracture under the joint impact of bedding planes and natural fractures in shale reservoirs", *Energ. Sci. Eng*., **7**, 2690-2702. https://doi.org/10.1002/ese3.453.

Guo, Y.T., Yang, C.H., Wang, L. and Xu, F. (2018), "Study on the influence of bedding density on hydraulic fracturing in shale", *Arab. J. Sci. Eng*., **43**, 6493-6508. https://doi.org/10.1007/s13369-018-3263-6.

Haeri, H. (2015a), "Erratum to: "Propagation mechanism of neighboring cracks in rock-like cylindrical specimens under uniaxial compression", *J. Min. Sci*., **51**, 1062. https://doi.org/10.1134/S1062739115040296.

Haeri, H. (2015b), "Experimental crack analyses of concrete-like CSCBD specimens using a higher order DDM", *Comput. Concrete*, **16**(6), 881-896. https://doi.org/10.12989/cac.2015.16.6.881.

Haeri, H. (2015c), "Simulating the crack propagation mechanism of pre-cracked concrete specimens under shear loading conditions", *Strength of Mater*., **47**(4), 618-632. https://doi.org/10.1007/s11223-015-9711-6.

Haeri, H., Sarfarazi, V. and Marji M.F. (2020), "Numerical simulation of the effect of confining pressure and tunnel depth on the vertical settlement using particle flow code (with direct tensile strength calibration in PFC Modeling)", *Smart Struct. Syst*., **25**(4), 433-446. https://doi.org/10.12989/sss.2020.25.4.433.

Huang, B.X. and Liu, J.W. (2017), "Experimental investigation of the effect of bedding planes on hydraulic fracturing under true triaxial stress", *Rock Mech. Rock Eng*., **50**, 2627-2643. https://doi.org/10.1007/s00603-017-1261-8.

Imani, M., Nejati, H.R., Goshtasbi, K. and Nazerigivi, A. (2022), "Effect of brittleness on the micromechanical damage and failure pattern of rock specimens", *Smart Struct. Syst*., **29**(4), 535-547. https://doi.org/10.12989/sss.2022.29.4.535.

Li, J., Zou, Y., Shi, S., Zhang, S., Wang, J., Ma, X. and Zhang, X. (2022), "Experimental study on fracture propagation mechanism of shale oil reservoir of Lucaogou Formation in Jimusar", *Geofluids,* 6598575. https://doi.org/10.1155/2022/6598575.

Li, Y., Hu, W., Zhang, Z., Zhang, Z., Shang, Y., Han, L. and Wei, S. (2021), "Numerical simulation of hydraulic fracturing process in a naturally fractured reservoir based on a discrete fracture network model", *J. Struct. Geol*., **147**, 104331. https://doi.org/10.1016/j.jsg.2021.104331.

Men, X., Tang, C.a., Wang, S., Li, Y., Yang, T. and Ma, T. (2013), "Numerical simulation of hydraulic fracturing in heterogeneous rock: The effect of perforation angles and bedding plane on hydraulic fractures evolutions", *Proceedings of the SRM International Conference for Effective and Sustainable Hydraulic Fracturing, Brisbane*, QLD, Australia. https://doi.org/10.5772/56012.

Munoz-Abella, B., Rubio, L. and Rubio, P. (2012), "A non-destructive method for elliptical cracks identification in shafts based on wave propagation signals and genetic algorithms", *Smart Struct. Syst*., **10**(1), 47-65. https://doi.org/10.12989/sss.2012.10.1.047.

Naeimi, N., Bagher Tavakoli, M. and Sabbaghi-Nadooshan, R. (2021), "Design of non-volatile digital circuit with assuming magnetic tunneling junction and carbon nanotubes field-effect transistors devices", *Smart Struct. Syst*., **27**(6), 983-990. https://doi.org/10.12989/sss.2021.27.6.983.

Öner, E., Şengül Şabano, B., Uzun Yaylacı, E., Adıyaman, G., Yaylacı, M. and Birinci, A. (2022), "On the plane receding contact between two functionally graded layers using computational, finite element and artificial neural network methods", *J. Appl. Math. Mech. (ZAMM)*, **102**, e202100287. https://doi.org/10.1002/zamm.202100287.

Öner, E., Yaylacı, M. and Birinci, A. (2014), "Solution of a receding contact problem using an analytical method and a finite element method", *J. Mech. Mater. Struct*., **9**, 333-345.

Sadd, M. (2020), *Elasticity: Theory, Applications, and Numerics*

(4th Ed.). Academic Press.
Sarfarazi, V., Abharian, S. and Zarin Ghalam, E. (2021), "Physical test and PFC2D simulation of the failure mechanism of echelon joint under uniaxial compression", *Comput. Concrete*, **27**(2), 99-109. https://doi.org/10.12989/cac.2021.27.2.099.
Selmi, A. (2022), "Dynamic behavior of cracked ceramic reinforced aluminum composite beam", *Smart Struct. Syst*., **29**(3), 387-393. https://doi.org/10.12989/sss.2022.29.3.387.
Shaowei, H., Aiqing, X., Xin, H. and Yangyang, Y. (2016), "Study on fracture characteristics of reinforced concrete wedge splitting tests", *Comput. Concrete*., **18**(3), 337-354. https://doi.org/10.12989/cac.2016.18.3.337.
Shuraim, A.B., Aslam, F., Hussain, R. and Alhozaimy, A. (2016), "Analysis of punching shear in high strength RC panels–experiments, comparison with codes and FEM results", *Comput. Concrete*., **17**(6), 739-760. https://doi.org/10.12989/cac.2016.17.6.739.
Sun, C., Zheng, H., Liu, W.D. and Lu, W. (2020), "Numerical simulation analysis of vertical propagation of hydraulic fracture in bedding plane", *Eng. Fract. Mech*., **232**, 107056. https://doi.org/10.1016/j.engfracmech.2020.107056.
Tang, J., Wu, K., Li, Y., Hu, X., Liu, Q. and Ehlig-Economides, C. (2018), "Numerical investigation of the interactions between hydraulic fracture and bedding planes with non-orthogonal approach angle", *Eng. Fract. Mech*., **200**, 1-16. https://doi.org/10.1016/j.engfracmech.2018.07.010.
Weng, X., Chuprakov, D., Kresse, O., Prioul, R. and Wang, H. (2018), "Hydraulic fracture-height containment by permeable weak bedding interfaces", *Geophysics*, **83**, MR137–MR152. https://doi.org/10.1190/geo2017-0048.1.
Woo, J., Kim, D. and Na, W.B. (2015), "Application of numerical simulation of submersed rock-berm structure under anchor collision for structural health monitoring of submarine power cables", *Smart Struct. Syst*., **15**(2), 299-314. https://doi.org/10.12989/sss.2015.15.2.299.
Wu, S., Ge, H., Li, T., Wang, X., Li, N., Zou, Y. and Gao, K. (2022), "Characteristics of fractures stimulated by supercritical carbon dioxide fracturing in shale based on acoustic emission monitoring", *Int. J. Rock Mech. Min. Sci*., **152**, 105065. https://doi.org/10.1016/j.ijrmms.2022.105065.
Xie, J., Tang, J., Yong, R., Fan, Y., Zuo, L., Chen, X. and Li, Y. (2020), "A 3-D hydraulic fracture propagation model applied for shale gas reservoirs with multiple bedding planes", *Eng. Fract. Mech*., **228**, 106872. https://doi.org/10.1016/j.engfracmech.2020.106872.
Yaylacı, M. (2016), "The investigation crack problem through numerical analysis", *Struct. Eng. Mech*., **57**(6), 1143-1156. https://doi.org/10.12989/sem.2016.57.6.1143.
Zeng, Q. and Yao, J. (2016), "Numerical simulation of fracture network generation in naturally fractured reservoirs", *J. Nat. Gas Sci. Eng*., **30**, 430-443. https://doi.org/10.1016/j.jngse.2016.02.047.
Zhang, F., Dontsov, E. and Mack, M. (2017), "Fully coupled simulation of a hydraulic fracture interacting with natural fractures with a hybrid discrete-continuum method", *Int. J. Numer. Anal. Method. Geomech*., **41**, 1430-1452. https://doi.org/10.1002/nag.2682.
Zhao, Y., Zhang, Y., Wang, C. and Liu, Q. (2022), "Hydraulic fracturing characteristics and evaluation of fracturing effectiveness under different anisotropic angles and injection rates: An experimental investigation in absence of confining pressure", *J. Nat. Gas Sci. Eng*., **97**, 104343. https://doi.org/10.1016/j.jngse.2021.104343.
Zhou, J., Zhang, L., Braun, A. and Han, Z. (2017), "Investigation of processes of interaction between hydraulic and natural fractures by PFC modeling comparing against laboratory experiments and analytical models", *Energies*, **10**, 1001, https://doi.org/10.3390/en10071001.
Zou, Y., Ma, X., Zhang, S., Zhou, T. and Li, H. (2016), "Numerical investigation into the influence of bedding plane on hydraulic fracture network propagation in shale formations", *Rock Mech. Rock Eng*., **49**, 3597-3614. https://doi.org/10.1007/s00603-016-1001-5.

CC